The Journal of Chemical Physics

RESEARCH ARTICLE | MAY 09 2023

Solubility of carbon dioxide in water: Some useful results for hydrate nucleation

Special Collection: Nucleation: Current Understanding Approaching 150 Years After Gibbs

Jesús Algaba; Iván M. Zerón; José Manuel Míguez; ... et. al

Check for updates

J. Chem. Phys. 158, 184703 (2023)
https://doi.org/10.1063/5.0146618

View Online
Export Citation
CrossMark

Downloaded from http://pubs.aip.org/aip/jcp/article-pdf/doi/10.1063/5.0146618/17414902/184703_1_5.0146618.pdf

AIP Publishing

The Journal of Chemical Physics ARTICLE scitation.org/journal/jcp

Solubility of carbon dioxide in water: Some useful results for hydrate nucleation

Cite as: J. Chem. Phys. 158, 184703 (2023); doi: 10.1063/5.0146618
Submitted: 15 February 2023 • Accepted: 18 April 2023 •
Published Online: 9 May 2023

View Online Export Citation CrossMark

Jesús Algaba,[1] Iván M. Zerón,[1] José Manuel Míguez,[1] Joanna Grabowska,[2,3] Samuel Blazquez,[3] Eduardo Sanz,[3] Carlos Vega,[3] and Felipe J. Blas[1,a)]

AFFILIATIONS

[1] Laboratorio de Simulación Molecular y Química Computacional, CIQSO-Centro de Investigación en Química Sostenible and Departamento de Ciencias Integradas, Universidad de Huelva, 21006 Huelva, Spain
[2] Department of Physical Chemistry, Faculty of Chemistry and BioTechMed Center, Gdansk University of Technology, ul. Narutowicza 11/12, 80-233 Gdansk, Poland
[3] Dpto. Química Física, Fac. Ciencias Químicas, Universidad Complutense de Madrid, 28040 Madrid, Spain

Note: This paper is part of the JCP Special Topic on Nucleation: Current Understanding Approaching 150 Years After Gibbs.
[a)] **Author to whom correspondence should be addressed:** felipe@uhu.es

ABSTRACT

In this paper, the solubility of carbon dioxide (CO_2) in water along the isobar of 400 bar is determined by computer simulations using the well-known TIP4P/Ice force field for water and the TraPPE model for CO_2. In particular, the solubility of CO_2 in water when in contact with the CO_2 liquid phase and the solubility of CO_2 in water when in contact with the hydrate have been determined. The solubility of CO_2 in a liquid–liquid system decreases as the temperature increases. The solubility of CO_2 in a hydrate–liquid system increases with temperature. The two curves intersect at a certain temperature that determines the dissociation temperature of the hydrate at 400 bar (T_3). We compare the predictions with T_3 obtained using the direct coexistence technique in a previous work. The results of both methods agree, and we suggest 290(2) K as the value of T_3 for this system using the same cutoff distance for dispersive interactions. We also propose a novel and alternative route to evaluate the change in chemical potential for the formation of hydrates along the isobar. The new approach is based on the use of the solubility curve of CO_2 when the aqueous solution is in contact with the hydrate phase. It considers rigorously the non-ideality of the aqueous solution of CO_2, providing reliable values for the driving force for nucleation of hydrates in good agreement with other thermodynamic routes used. It is shown that the driving force for hydrate nucleation at 400 bar is larger for the methane hydrate than for the carbon dioxide hydrate when compared at the same supercooling. We have also analyzed and discussed the effect of the cutoff distance of dispersive interactions and the occupancy of CO_2 on the driving force for nucleation of the hydrate.

Published under an exclusive license by AIP Publishing. https://doi.org/10.1063/5.0146618

I. INTRODUCTION

Under ambient conditions of temperature and pressure (298 K and 1 bar), the thermodynamically stable phase of water is the liquid phase. If the temperature is decreased at a constant pressure of 1 bar, the liquid is no longer the most stable phase and a first-order phase transition takes place at 273.15 K. Consequently, and according to thermodynamics laws, water must freeze. The new thermodynamically stable phase is the well-known ordinary ice, also known as Ih or hexagonal ice. This solid phase is formed by a crystalline structure characterized by oxygen atoms forming hexagonal symmetry with nearly tetrahedral bonding angles. The same happens if the pressure is above ambient conditions up to 2100 bar, approximately. Above this pressure, water can freeze into other ices, including ices III, V, and VI, among others, as the pressure is increased.[1–3] These are only some of the solid crystalline phases of the well-known polymorphic phases of water. However, this only happens if the original liquid phase is formed from pure water. When liquid water is mixed with another substance, the story can be different.

There exist aqueous solutions of small compounds that exhibit different behavior when cooled down at constant pressure. Particularly, aqueous solutions of methane (CH_4), carbon dioxide (CO_2), nitrogen (N_2), hydrogen (H_2), or larger organic molecules, among many other different compounds, do not transform into

Downloaded from http://pubs.aip.org/aip/jcp/article-pdf/doi/10.1063/5.0146618/17414902/184703_1_5.0146618.pdf

Published under an exclusive license by AIP Publishing

a crystalline ice phase when the temperature is lowered. In fact, all these aqueous solutions freeze into new crystalline solid compounds named clathrate hydrates or simply hydrates.[4] Hydrates are non-stoichiometric crystalline inclusion compounds consisting of a network of hydrogen-bonding water molecules forming cages in which small molecules (for instance, CH_4, CO_2, N_2, or H_2) are enclathrated at appropriate thermodynamic conditions of temperature and pressure.

Fundamental and applied research on hydrates and clathrates has been motivated by several reasons. First of all, hydrates are potential alternative sources of energy since huge amounts of CH_4 have been identified in hydrate deposits either in the sea floor or in permafrost frozen substrates, but their exploitation is not technically accessible yet due to a poor physicochemical characterization and various engineering issues.[5,6] Another remarkably relevant aspect of hydrates from both the scientific point of view and practical interest is the possibility to capture[7,8] and store CO_2.[9] This places gas hydrates at the center of environmental concerns regarding atmospheric greenhouse gases. Sequestration and capture of CO_2 in hydrates constitute a technological breakthrough, which is seen as a promising alternative to other conventional methodologies for CO_2 capture, such as reactive absorption using amines and selective adsorption using adsorbent porous materials, including sieves and zeolites.[10,11]

It is clear from the previous discussion that an accurate knowledge of the thermodynamics and kinetics of the formation and growth of hydrates is necessary from the fundamental and practical points of view. The thermodynamics of hydrates has been relatively well-established experimentally for years.[4] In addition, it is also possible to describe theoretically the phase equilibria of hydrates using the van der Waals and Platteeuw (vdW & P) formalism.[12,13] This approach, combined with an equation of state (EOS), allows us to satisfactorily determine the phase equilibrium of both pure hydrates and mixtures.[4] Additionally, from the point of view of molecular simulation, there has been an enormous development in techniques and methodologies for the study of the formation and dissociation of a huge variety of hydrates.[14–21] Particularly, several research groups have determined the phase equilibrium of CO_2[22,23] and CH_4 hydrates under oceanic crust conditions[24,25] using the direct coexistence technique. The precise knowledge of phase equilibria of hydrates, and particularly their phase boundaries, is essential to provide a detailed description of kinetic and nucleation processes of these systems.

Unfortunately, a complete description from a molecular perspective of the mechanisms of growth and hydrate formation is far from being satisfactory. In the last few years, some of the authors of this work have been working on the development and use of the Seeding Technique,[26] in combination with the Classical Nucleation Theory (CNT),[27] to deal with several systems, including the hard-sphere and Lennard-Jones (LJ) models and more complex systems, such as water and salty water.[28] More recently, we have extended the study to deal with methane hydrates.[29,30] It is important to recall here that Molinero *et al.* the used Seeding Technique to estimate nucleation rates of hydrates[31] modeled through the well-known mW water model.[32] Other authors have also contributed significantly to the understanding of the dynamics of nucleation and dissociation of hydrates from computer simulation.[33–50] This work constitutes the extension of our most recent study[29] on methane hydrates to deal with CO_2 hydrates. Before undertaking nucleation studies of CO_2 hydrates, it is necessary to account for several issues, including the solubility of CO_2 in the aqueous solution when it is in contact with the CO_2-rich liquid phase and with the hydrate, an accurate prediction of the dissociation temperature, and the driving force for nucleation.

The phase behavior of the CO_2 + water binary mixture is dominated by a large region of liquid–liquid (L_w–L_{CO_2}) immiscibility.[51] Since the critical point of pure CO_2 and a liquid–liquid–vapor (L_w–L_{CO_2}–V) three-phase line are at conditions similar to those at which the CO_2 hydrates are found, between 270 and 295 K and 10–5000 bar, approximately, another three-phase coexistence line involving a hydrate phase (i.e., a triple point that occurs at a certain temperature T_3 for each pressure) exhibits two branches. This is contrary to what happens with methane hydrates, which only exhibit one branch.[4] Figure 1 shows the pressure–temperature (PT) projection of the phase diagram of the CO_2 + water binary mixture. At pressures below 44.99 bar, the dissociation line is a H–L_w–V three-phase line at which the hydrate, the aqueous solution of CO_2, and the vapor phases coexist. Above that pressure, the hydrate and the solution coexist with a CO_2 liquid phase and a three-phase H–L_w–L_{CO_2} line where the hydrate, the aqueous solution of CO_2, and the liquid phase of CO_2 coexist starts. Both branches meet at a Q_2 quadruple point located at 283 K and 44.99 bar (black filled circle) at which the hydrate, the aqueous solution, the CO_2 liquid, and the vapor phases coexist,[4] as can be seen in Fig. 1. Note that at Q_2, the L_w–L_{CO_2}–V three-phase line also meets with another H–L_{CO_2}–V three-phase in which the hydrate, the CO_2 liquid, and the vapor phases coexist at lower temperatures. In addition to this, there exists another quadruple point Q_1, located at 273 K and 12.56 bar (black filled square), at which the hydrate, the Ih ice, the solution, and the vapor phases coexist. This quadruple point connects the H–L_w–V three-phase line

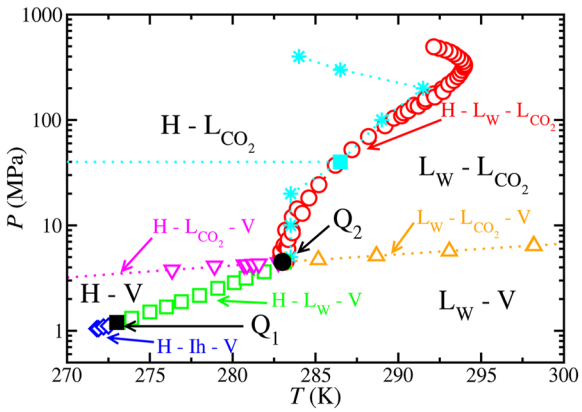

FIG. 1. *PT* projection of the phase diagram of the CO_2 + water mixture. The open symbols represent the experimental three-phase lines for the H–L_w–L_{CO_2} (red circles),[4] H–L_w–V (green squares),[4] H–Ih–V (blue diamonds),[4] L_w–L_{CO_2}–V (orange up triangles),[4] and L_w–L_{CO_2}–V (magenta down triangles)[4] equilibria. The black square and the black circle are the experimental quadruple points Q_1 and Q_2,[4] respectively. Cyan stars correspond to the simulation results obtained by Míguez *et al.*[22] for the H–L_w–L_{CO_2} three-phase line. The cyan filled square represents the state at T_3 and 400 bar as obtained in this work. The horizontal cyan dotted line represents the 400 bar isobar at which the driving force for nucleation is evaluated in this work. The rest of lines are guides to the eye.

Downloaded from http://pubs.aip.org/aip/jcp/article-pdf/doi/10.1063/5.0146618/17414902/184703_1_5.0146618.pdf

Published under an exclusive license by AIP Publishing

with a new three-phase H–Ih–V line involving the hydrate, the Ih ice, and the vapor phases that runs toward lower temperatures and pressures.

In this work, we concentrate on 400 bar of pressure (see the 400 bar isobar in Fig. 1 along which all the simulations are performed). At these conditions, the key solubility curves in the context of nucleation of CO_2 hydrates are the solubility of CO_2 in water when the aqueous solution is in contact with the CO_2 liquid phase or with the hydrate phase. In the first case, the solubility of CO_2 increases as the temperature is decreased. In the second case, as it occurs for the methane hydrate, there is little or no information from computer simulations or experiments. Here, we determine the solubility of CO_2 in water from the hydrate along the isobar of 400 bar. This will allow us to estimate the dissociation line of the hydrate at this pressure, as we have done in our previous work for the case of the methane hydrate.[29]

The dissociation line of the CO_2 hydrate has been already determined by us several years ago.[22] It is important to mention that other authors also have obtained similar results using computer simulations[17] and free energy calculations.[19] Our previous results are slightly different from those found by Costandy *et al.*[17] and Waage *et al.*[19] since unlike dispersive interactions between water and CO_2 are different. However, we follow our previous work[29] and determine the dissociation line of the hydrate using the solubility curve of CO_2 in the aqueous solution when it is in contact with the CO_2 liquid phase and the hydrate. We have found that our new estimations agree with the initial prediction of Míguez *et al.*[22] within the corresponding uncertainties.

The formation of the CO_2 hydrate can be viewed as a chemical reaction in which water and CO_2 molecules "react" in the aqueous solution phase to form hydrate molecules.[52–55] The change in chemical potential of this reaction is the driving force for nucleation, $\Delta\mu_N$. It is difficult to get good estimates of $\Delta\mu_N$ from experiments since it requires accurate values for a number of thermodynamic properties.[53] Here, we use the three independent routes introduced in our previous paper[29] to deal with the nucleation driving force for the nucleation of CO_2 hydrates. Particularly, we calculate the driving force for nucleation with respect to the state on the $H–L_w–L_{CO_2}$ three-phase line at 400 bar. Note that this point is well above the two quadruple points Q_1 and Q_2 shown in Fig. 1. In addition to this, we also propose a novel and alternative thermodynamic route based on the use of the solubility curve of CO_2 with the hydrate. This new route, which considers rigorously the non-ideality of the aqueous solution of CO_2 and provides reliable results of the driving force for nucleation, can also be used to determine $\Delta\mu_N$ of other hydrates.

The organization of this paper is as follows. In Sec. II, we describe the methodology used in this work. The results obtained, as well as their discussion, are described in Sec. III. Finally, conclusions are presented in Sec. IV.

II. METHODOLOGY

We use the GROMACS simulation package[56] to perform molecular dynamics (MD) simulations. Computer simulations have been performed using three different versions of the *NPT* or isothermal–isobaric ensemble. For pure systems that exhibit fluid phases (pure water and pure CO_2) and aqueous solutions of CO_2 that exhibit bulk phases, we use the standard isotropic *NPT* ensemble, i.e., the three sides of the simulation box are changed proportionally to keep the pressure constant. For the hydrate phase, we use the anisotropic *NPT* ensemble in which each side of the simulation box is allowed to fluctuate independently to keep the pressure constant. This ensures that the equilibrated solid phase has no stress and that the thermodynamic properties are correctly estimated. The same ensemble is used to simulate the two-phase equilibrium between the hydrate and the aqueous solution of CO_2 (SL coexistence). Finally, the two-phase equilibrium between the solution and the CO_2 liquid phase is obtained using the $NP_z\mathscr{A}T$ ensemble in which only the side of the simulation box perpendicular to the liquid–liquid (LL) planar interface is allowed to change, with the interface area kept constant, to keep the pressure constant. For simulations involving LL and SL interfaces, we have used sufficiently large values of interfacial areas $\mathscr{A}$. The thermodynamics and interfacial properties obtained from simulations of LL interfaces do not show a dependence on the surface area for systems with $\mathscr{A} > 10 \times 10\,\sigma^2$.[57–59] Here, σ is the largest Lennard-Jones diameter of the intermolecular potentials. In all simulations, the $\mathscr{A}$ values used are higher than this value for LL and SL interfaces. See Secs. III A and III C for the particular values used in this work.

In all simulations, we use the Verlet leapfrog[60] algorithm with a time steps of 2 fs. We use a Nosé–Hoover thermostat[61] with a coupling time of 2 ps to keep the temperature constant. In addition to this, we also use the Parrinello–Rahman barostat[62] with a time constant equal to 2 ps to keep the pressure constant. We use two different cutoff distances for the dispersive and Coulombic interactions, r_c = 1.0 and 1.9 nm. We use periodic boundary conditions in all three dimensions. The water–water, $CO_2–CO_2$, and water–CO_2 long-range interactions due to Coulombic forces are determined using the three-dimensional Ewald technique.[63] Particularly, the real part of the Coulombic potential is truncated at the same cutoff as dispersive interactions. The Fourier term of the Ewald sums is evaluated using the particle mesh Ewald (PME) method. The width of the mesh is 0.1 nm with a relative tolerance of 10^{-5}. In some calculations, we also use the standard long-range corrections for the LJ part of the potential to energy and pressure with r_c = 1.0 nm. Water molecules are modeled using the TIP4P/Ice model,[64] and the CO_2 molecules are described using the TraPPE model.[65] The $H_2O–CO_2$ unlike dispersive energy value is given by the modified Berthelot combining rule, $\varepsilon_{12} = \xi(\varepsilon_{11}\,\varepsilon_{22})^{1/2}$ with ξ = 1.13. This is the same used by Míguez *et al.*,[22] which allows us to predict accurately the three-phase hydrate–water–carbon dioxide coexistence or dissociation line of the CO_2 hydrate, particularly the coexistence temperature at the pressure considered in this work, 400 bar (see Fig. 10 and Table II of the work of Míguez *et al.* for further details). Very recently, we have demonstrated that the same molecular parameters are able to predict accurately the CO_2 hydrate–water interfacial free energy.[66,67]

Finally, uncertainties are estimated using the standard deviation of mean values or sub-block average method. Particularly, bulk densities in the LL and SL coexistence studies are obtained by averaging the corresponding density profiles over the appropriate regions sufficiently away from the interfacial regions. The statistical uncertainties of these values are estimated from the standard deviation of the mean values. Solubilities of CO_2 in all the liquid phases are calculated as molar fractions from the densities of both components, and the corresponding errors are obtained from propagation of

Downloaded from http://pubs.aip.org/aip/jcp/article-pdf/doi/10.1063/5.0146618/17414902/184703_1_5.0146618.pdf

Published under an exclusive license by AIP Publishing

uncertainty formulas. Uncertainties associated with LL interfacial tension values, molar enthalpies, and partial molar enthalpies are estimated using the standard sub-block average method. Particularly, the production periods are divided into ten (independent) blocks. The statistical errors are estimated from the standard deviation of the average.

III. RESULTS

A. Solubility of carbon dioxide in water from the CO_2 liquid phase

We first concentrate on the solubility of CO_2 in the aqueous solution when the system exhibits LL immiscibility. In this case, there exists a coexistence between the water-rich and CO_2 liquid phases. We have used the direct coexistence technique to determine the solubility of CO_2 in the aqueous solution from the CO_2 liquid phase at several temperatures along the 400 bar isobar. Particularly, we have performed MD $NP_z\mathscr{A}T$ simulations to ensure that temperature and pressure are constant. According to this, the planar interfacial area $\mathscr{A} = L_x \times L_y$ is kept constant and only L_z is varied along each simulation. Here, L_x, L_y, and L_z are the dimensions of the simulation box along the x, y, and z axis, respectively. In this work, the z axis is chosen to be perpendicular to the planar interface. The initial simulation box is prepared in the following way. We build a slab of 2800 water molecules in contact, via a planar interface, with a second slab of 1223 molecules of CO_2. The dimensions of L_x and L_y of all the simulation boxes used in this part of the work are kept constant with $L_x = L_y = 3.8$ nm ($\mathscr{A} \simeq 12 \times 12\,\sigma^2$). Since the pressure is constant, L_z varies along each simulation for all the temperatures considered. In this work, L_z varies from 11.06 to 12.29 nm. Simulations to calculate solubilities are run during 100 ns. The first 20 ns are used to equilibrate the system, and the last 80 ns are used as the production period to obtain the properties of interest. We have also determined the LL interfacial tension, and details of simulations are explained later in this section.

Figure 2 shows the density profiles of water and CO_2 as obtained by MD $NP_z\mathscr{A}T$ simulations at 400 bar and temperatures from 250 to 310 K. For a better visualization for the reader, we only plot half of the profiles corresponding to one of the interfaces exhibited by the system. The right side of Fig. 2 corresponds to the CO_2 liquid phase and the left side to the aqueous liquid phase. We divide the inhomogeneous simulation box into 200 parallel slabs along the z direction, perpendicular to the planar LL interface, to study the density profiles. Following the standard approach, density profiles are obtained assigning the position of each interacting site to the corresponding slab and constructing the molecular density from mass balance considerations.

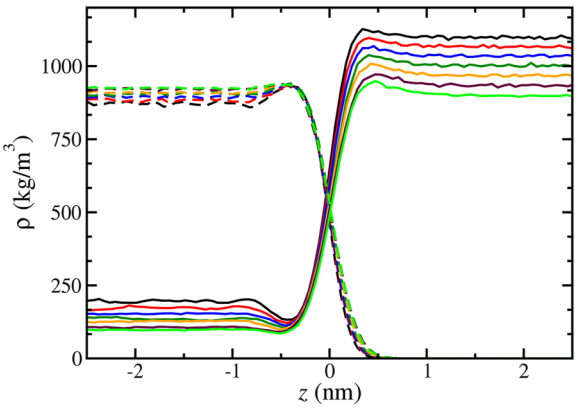

FIG. 2. Simulated equilibrium density profiles, $\rho(z)$, across the LL interface of CO_2 (continuous curves) and water (dashed curves) as obtained from MD $NP_z\mathscr{A}T$ simulations at 400 bar and 250 (black), 260 (red), 270 (blue), 280 (dark green), 290 (orange), 300 (maroon), and 310 K (green).

As can be seen, density profiles of water (dashed curves) exhibit preferential adsorption at the interface at all temperatures. Particularly, water molecules are accumulated at the aqueous phase side of the interface. The relative maximum, which is identified with the accumulation of the water molecules, increases as the temperature of the system is decreased. The bulk density of water in the aqueous solution of CO_2 (left side of Fig. 2) slightly decreases as the temperature is lower, especially in the range of 250–290 K. As can be seen, density profiles of water are nearly equal to zero at the bulk CO_2 liquid phase, indicating that solubility of water in that phase is completely negligible. Míguez *et al.*[68] previously studied the LL interface of aqueous solutions of CO_2 at similar temperatures (287 and 298 K) but at lower pressures ($P \leq 55$ bar). These authors have found similar behavior for the density profiles of water but with an important exception: they exhibit the traditional shape of the hyperbolic tangent function in which water density decreases monotonically from the bulk density of water in the aqueous phase to zero in the CO_2 liquid phase.

The behavior and structure of the density profiles of CO_2 (continuous curves) along the interface are similar to those exhibited by other mixtures but with an important exception: CO_2 molecules exhibit activity on both sides of the liquid–liquid interface of the system. Particularly, there is an accumulation of CO_2 molecules at the CO_2 liquid phase side of the interface. This accumulation increases as the temperature of the system is decreased, as it happens with water molecules on the other side of the interface. The bulk density of CO_2 in both phases increases as the temperature is increased. This variation is more important in the CO_2 liquid phase (right side of Fig. 2). Contrary to what happens with water density in the CO_2 phase, the density of CO_2 in the aqueous solution is not negligible. This indicates that although the solubility of CO_2 in water is small (molar fraction of CO_2 between 0.04 and 0.09 in the range 310–250 K, respectively), its value is not so low as in the case of the solubility of water in CO_2.

It is interesting to mention that density profiles of CO_2 also exhibit depressions in the aqueous solution side of the interface, indicating desorption of CO_2 molecules in this region. The desorption of CO_2 molecules at the interface is correlated with the preferential adsorption of water molecules since the relative maxima and minima occur at the same position ($z \approx -0.45$ nm). Note that preferential adsorption and desorption of CO_2 molecules at the LL interface of this kind of aqueous solution has not been previously seen in the literature. Particularly, Míguez *et al.*[68] only observed density profiles that exhibit preferential adsorption at the interface.

The solubilities of CO_2 in the aqueous phase have been determined from the information of the density profiles represented in Fig. 2 at the corresponding temperatures. Figure 3 shows the solu-

Downloaded from http://pubs.aip.org/aip/jcp/article-pdf/doi/10.1063/5.0146618/17414902/184703_1_5.0146618.pdf

Published under an exclusive license by AIP Publishing

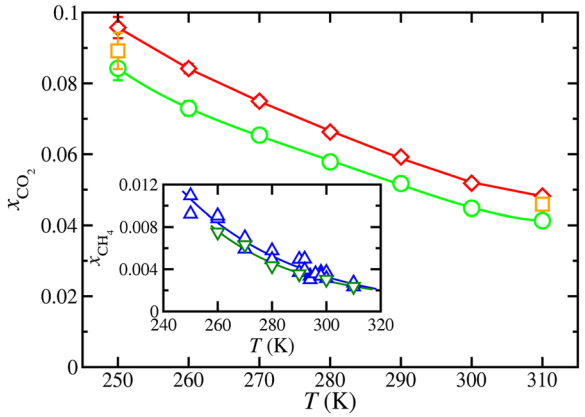

FIG. 3. Solubility of CO_2 in the aqueous phase, as a function of temperature, at 400 bar when the solution is in contact with the CO_2 liquid phase via a planar interface. The symbols correspond to solubility values obtained from MD $NP_z\mathscr{A}T$ simulations using cutoffs of 1.0 (green circles) and 1.9 nm (red diamonds). Orange squares correspond to simulation results using a cutoff of 1.0 nm and long-range corrections. Inset: solubility of methane in water, as a function of temperature, at 400 bar when the solution is in contact with the methane gas phase via a planar interface. Solubility values of methane in water are taken from our previous work.[29] Simulations are performed at the same conditions using cutoffs of 0.9 nm (blue triangles up) and 1.7 nm (dark green triangles down). In all cases, the curves are included as guides to the eyes.

bilities of CO_2 along the isobar at the temperatures considered. We have also included in Fig. 3 (inset) the same results obtained previously by us corresponding to the methane + water system.[29] As can be seen, the solubility decreases as the temperature increases. This result is in agreement with our previous work in which we considered the solubility of methane in water along the same isobar (400 bar) and in contact with the gas phase (see the inset).[29] In this work, the study is first done using a relatively short cutoff distance for dispersive interactions, r_c = 1.0 nm, which corresponds to a reduced cutoff value of $r^* = r_c/\sigma \cong 3.16$ with σ = 0.316 68 nm. Here, σ is the length scale of Lennard-Jones intermolecular interactions associated with the water model (TIP4P/Ice).[64] In order to evaluate the effect of the cutoff distance, we have also determined the solubility of CO_2 using a larger cutoff value for dispersive interactions (1.9 nm instead of 1.0 nm). As can be seen, the effect of increasing the cutoff is important in the whole range of temperatures considered. In particular, solubility increases between 17%, at high temperatures (310 K), and 13% at low temperatures (250 K). This is an expected result according to previous studies of the effect of the cutoff distance on fluid–fluid coexistence.[69–71]

We have checked that there is no *a priori* temperature limit to perform simulations as the temperature is decreased. From this point of view, the solubility of CO_2 in the aqueous solution can be computed without any difficulty since we do not observe nucleation of the hydrate up to the lowest temperature considered in this work (i.e., 250 K). This is in agreement with previous results obtained by Grabowska *et al.*[29] However, as the temperature is decreased, the dynamics of the system slows down and the equilibration of the LL interface becomes more difficult, and longer simulation runs are required to achieve equilibrated density profiles.

We have also determined the solubility using standard long-range corrections (LRC) to energy and pressure to the Lennard-Jones part of the potential (dispersive interactions). According to our results, although long-range corrections are able to improve the solubility results, differences between these results and those obtained with a cutoff of 1.9 nm are still noticeable. In particular, the solubilities predicted using this approach are underestimated (with respect to the results obtained with a cutoff of 1.9 nm) between 4% and 6% along the isobar at the two temperatures considered. It is interesting to compare the behavior of the CO_2 solubility, as a function of the temperature along 400 bar, with that corresponding to methane obtained by us previously.[29] As can be seen in the inset of Fig. 3, the effect of the long-range correction on dispersive interactions is slightly larger in the case of CO_2 than in methane. This is an expected result since the CO_2 molecules are modeled using three Lennard-Jones interaction sites and methane only with one and also because the solubility of CO_2 is about ten times higher than the CH_4 solubility at the same thermodynamic conditions. It is also remarkable that the use of longer cutoff distances has a contrary effect on the solubility of CO_2 than on that of methane, i.e., the solubility of CO_2 increases with an increase of the cutoff, whereas it decreases in the case of the solubility of methane. Further work is needed to determine if this is due to the significant different of densities between CO_2 (liquid) and methane (gas) or to water–CO_2 interactions that include a contribution from the quadrupole of CO_2 not present in CH_4.

In the previous paragraphs, we have presented and discussed the results corresponding to the solubility of CO_2 in the aqueous solution when it is in contact with the CO_2 liquid phase. Since both phases are in contact through a planar LL interface and are in equilibrium at the same P and T, the chemical potential of water and CO_2 in both phases must satisfied that

$$\mu^I_{CO_2}(P,T,x^I_{CO_2}) = \mu^{II}_{CO_2}(P,T,x^{II}_{CO_2}) \tag{1}$$

and

$$\mu^I_{H_2O}(P,T,x^I_{CO_2}) = \mu^{II}_{H_2O}(P,T,x^{II}_{CO_2}). \tag{2}$$

Here, the superscripts I and II label the aqueous and CO_2 liquid phases, respectively. Note that we have expressed the chemical potential of water in each phase in terms of the corresponding CO_2 molar fractions. It is important to note that this is consistent from the thermodynamic point of view, and it is always possible since we are dealing with a binary system that exhibits two-phase equilibrium. Following the Gibbs phase rule, such a system has two degrees of freedom, which according to Eqs. (1) and (2) are P and T. Consequently, the thermodynamic behavior of the system is fully described solving the previous equations since the composition of water in both phases, $x^I_{H_2O}$ and $x^{II}_{H_2O}$, can be readily obtained as $x^I_{H_2O} = 1 - x^I_{CO_2}$ and $x^{II}_{H_2O} = 1 - x^{II}_{CO_2}$.

According to our previous results shown in Fig. 2, the density of water in the CO_2 liquid phase is $\rho^{II}_{H_2O} \approx 0$, and consequently, $x^{II}_{H_2O} = \rho^{II}_{H_2O}/(\rho^{II}_{H_2O} + \rho^{II}_{CO_2}) \approx 0$ and $x^{II}_{CO_2} = 1 - X^{II}_{H_2O} \approx 1$.

Following the approximations of the previous paragraph combined with Eq. (1), the chemical potential of CO_2 in the aqueous solution can be obtained from the chemical potential of pure CO_2 at the same P and T,

Downloaded from http://pubs.aip.org/aip/jcp/article-pdf/doi/10.1063/5.0146618/17414902/184703_1_5.0146618.pdf

Published under an exclusive license by AIP Publishing

$$\mu^{I}_{CO_2}(P,T,x^{I}_{CO_2}) \approx \mu^{II}_{CO_2}(P,T,x^{II}_{CO_2} \approx 1) \approx \mu^{II}_{CO_2}(P,T). \quad (3)$$

The chemical potential of CO_2 along the isobar can be obtained from the thermodynamic relation,

$$\left(\frac{\partial(\mu_{CO_2}/T)}{\partial T}\right)_{P,N_{H_2O},N_{CO_2}} = -\frac{h_{CO_2}}{T^2}, \quad (4)$$

where $h_{CO_2} = h_{CO_2}(P,T)$ is the partial molar enthalpy of CO_2 and the derivative is performed at constant pressure, P, and number of water and CO_2 molecules, N_{H_2O} and N_{CO_2}, respectively. Since in our case the CO_2 liquid phase is essentially a pure CO_2 liquid, h_{CO_2} is simply the molar enthalpy. Consequently, the chemical potential of CO_2, as a function of the temperature, along the 400 bar isobar can be obtained by integrating Eq. (4) as

$$\frac{\mu_{CO_2}(T)}{k_BT} = \frac{\mu_{CO_2}(T_0)}{k_BT_0} - \int_{T_0}^{T} \frac{h_{CO_2}(T')}{k_BT'^2}\,dT', \quad (5)$$

where k_B is the Boltzmann constant and T_0 is a certain reference temperature. Following our previous work,[29] we set $\mu_{CO_2}(T_0) = 0$. According to Eq. (5), $\mu_{CO_2}(T)$ can be obtained by performing MD NPT simulations of pure CO_2 along the 400 bar isobar. In this case, since we are simulating a bulk phase, the standard NPT is used in such a way that the three dimensions of the simulation box are allowed to fluctuate isotropically. We use a cubic simulation box with 1000 CO_2 molecules. The dimensions of the simulation box L_x, L_y, and L_z vary depending on the temperature from 3.9 to 4.2 nm. Simulations to calculate the molar enthalpy, at each temperature, are run during 100 ns, 20 ns to equilibrate the system and 80 ns as the production period to obtain h_{CO_2}. As in our previous work, we have not included in h_{CO_2} the kinetic energy contribution (i.e., $5/2k_BT$ in the case of a rigid diatomic molecule, such as CO_2). Note that this contribution is canceled out since we are evaluating chemical potential differences at constant P and T. In this work, we choose as the reference temperature $T_0 = 290$ K. The reason for this selection will be clear later in this article. Figure 4 shows the chemical potential of CO_2 as a function of the temperature (blue curve). We have also included in Fig. 4 the chemical potential values of bulk methane taken from our previous work[29] (green curve) in order to compare both chemical potentials. Note that the reference temperature at which μ of the bulk methane is set to zero is 295 K.

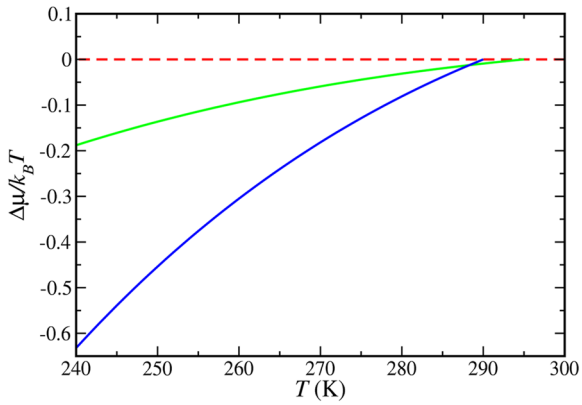

FIG. 4. Change of chemical potential, $\Delta\mu$, as a function of temperature, of bulk CO_2 (blue curve) and bulk methane (green curve) obtained along the isobar 400 bar. We have arbitrarily set the value of the chemical potential of CO_2 and methane to zero at 290 and 295 K, respectively. Chemical potential values of methane are taken from our previous work.[29]

B. LL interfacial free energy

From the same simulations, we have also obtained the LL interfacial tension, γ, from the diagonal components of the pressure tensor. The vapor pressure corresponds to the normal component, $P \equiv P_{zz}$, of the pressure tensor (which does not depend on the distance to the interface). The interfacial tension is obtained using the well-known combination of the normal component and the average of the tangential components $\langle P_{xx}\rangle$ and $\langle P_{yy}\rangle$ (note that P_{xx} and P_{yy} depend on the distance to the interface) through the mechanical route as[72–75]

$$\gamma = \frac{L_z}{2}\left[P_{zz} - \frac{\langle P_{xx}\rangle + \langle P_{yy}\rangle}{2}\right]. \quad (6)$$

In Eq. (6), the factor 1/2 reflects that during simulations, there exist two LL interfaces in the system, being L_z the size of the simulation box in the z direction perpendicular to the planar interface. Figure 5 shows the LL interfacial tension value as obtained from MD NP_zAT simulations. Results obtained in our previous work corresponding to the LL interfacial tension of the methane + water mixture are also shown in the inset of Fig. 5.[29] The interfacial tension decreases as the temperature is increased. We first calculate the interfacial tension using a cutoff value of 1.0 nm (green circles). In this case, we have used 50 ns for the equilibration period and 50 ns more for the production period in which the averages are calculated. Our results

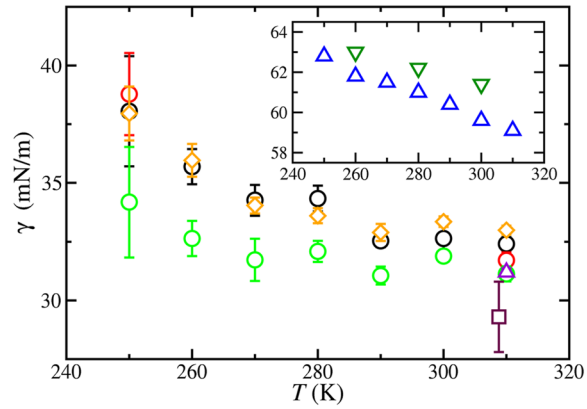

FIG. 5. LL interfacial tension, γ, as a function of the temperature between the CO_2 liquid phase and the aqueous solution at 400 bar obtained from MD NP_zAT simulations using cutoffs of 1.0 nm (black circles for 50 ns of equilibration and 50 ns of production, orange diamonds for 150 ns of equilibration, and 150 ns of production) and 1.9 nm (green circles for 50 ns of equilibration and 50 ns of production and violet triangle up for 150 ns of equilibration and 150 ns of production). Red circles correspond to simulation results using a cutoff of 1.0 nm and long-range corrections (50 ns of equilibration and 50 ns of production). The maroon square represents the experimental data taken from the literature.[76] Inset: LL interfacial tension values of the methane + water mixture at 400 bar taken from our previous work.[29] Simulations are performed at the same pressure and similar temperature conditions using cutoffs of 0.9 nm (blue triangles up) and 1.7 nm (dark green triangles down).

Downloaded from http://pubs.aip.org/aip/jcp/article-pdf/doi/10.1063/5.0146618/17414902/184703_1_5.0146618.pdf

Published under an exclusive license by AIP Publishing

indicate that the values exhibit large fluctuations, especially at low temperatures. To improve our results, we have extended simulations. The first 150 ns correspond to the equilibration period, and the extra 150 ns are used to obtain the corresponding average values (production period). As can be seen (green diamonds), although the mean values obtained in both cases are similar, the error bars decrease, especially at the lowest temperature.

It is well-known that the equilibrium interfacial tension value associated with an interface critically depends on the molecular details. In particular, its value is very sensitive to the cutoff due to the dispersive interactions used during simulations.[69,70,77–80] To account for long-range interactions associated with dispersive interactions, we have performed simulations using a cutoff distance of 1.9 nm, with 50 ns for equilibration and another 50 ns for production time (red circles). Note that in this case, we are not using long-range corrections to energy and pressure. This value corresponds to a reduced cutoff distance $r_c^* = r_c/\sigma = 6$, which is nearly the double value used in the first set of simulations. As can be seen, the main effect of increasing the cutoff distance is to decrease the interfacial tension values. Particularly, the effect is larger at low temperatures where the difference is about 3–4 mJ/m^2. However, at high temperatures, differences are about 1 mJ/m^2.

In order to account for the effect of the simulation length, we have extended simulation at 310 K. As in the other set of simulations, we have equilibrated the system during the first 150 and used the next 150 ns to perform the corresponding averages (red triangles up). As can be seen, the new results are, in practice, identical to those obtained using only 50 ns for production time.

To be consistent with the calculations of the solubility of CO_2 in the aqueous solution, we have also determined the interfacial tension using the traditional LRC to energy and pressure. As in the previous case, we have only simulated using these corrections at 250 and 310 K (orange circles). As can be seen, this approximation is not able to provide consistent results at low temperatures when compared with the data obtained using $r_c = 1.9$ nm. In particular, the interfacial tension is overestimated by more than 4.5 mJ/m^2, which represents more than 13% with respect to the value obtained using the larger cutoff distance. At the highest temperature, however, the overestimation of the interfacial tension is only about 0.5 mJ/m^2 (2%). Discrepancies at low temperatures between the results obtained using the largest cutoff distance (1.9 nm) and those using the traditional energy and pressure long-range corrections are probably due to the differences in densities in both liquid phases at these conditions.

We have also compared the predictions obtained from MD simulations with experimental data taken from the literature (maroon square).[76] Unfortunately, to the best of our knowledge, there are no experimental data below 310 K. Our results are in good agreement with experimental measurement although we slightly overestimate it by about 6%.

Finally, it is also interesting to compare the LL interfacial tension values obtained in this work for the CO_2 + water system with those obtained in our previous work[29] for the methane + water binary mixture. Computer simulation values of the former system are shown in the inset of Fig. 5. As can be seen, LL interfacial tension values of the methane + water system are approximately twice than those corresponding to the mixture containing CO_2. However, perhaps the most interesting feature is that, as it happens with the solubilities (see Fig. 3), an increase of the cutoff distance due to the dispersive interactions has the opposite effect in the systems that contain methane and CO_2: an increase of the cutoff distance in the CO_2 system lowers the LL interfacial tension values, while in the methane mixture, the interfacial tension values increase when the cutoff is larger (blue triangles up correspond to $r_c = 0.9$ nm and dark green triangles down to $r_c = 1.7$ nm). In addition, note that the effect of long-range dispersive contributions is more important in the CO_2 + water mixture than in the system containing methane. As discussed previously, further work is needed to understand the origin of that.

C. Solubility of carbon dioxide in water from the hydrate phase

We have also determined the solubility of CO_2 in water when the aqueous solution is in contact with the hydrate along the 400 bar isobar at several temperatures. We first prepare a simulation box of the CO_2 hydrate replicating a unit cell of hydrate four times along each spatial direction ($4 \times 4 \times 4$) using 2944 water and 512 CO_2 molecules. This corresponds to a hydrate with the cages (eight cages per unit cell) fully occupied by CO_2 molecules. We equilibrate the simulation box for 40 ns using an anisotropic barostat along the three axes. This allows the dimensions of the simulation box to change independently. The pressure is the same along the three directions and equal to 400 bar to allow the solid to relax and avoid any stress. In order to help the system to reach the equilibrium, we also prepare boxes of aqueous solutions with different concentrations of CO_2 depending on the temperature. This allows us to reach the equilibrium as fast as possible in the last stage of the simulations when the hydrate and liquid phases are put in contact (see below). Particularly, the hydrate phase will grow or melt depending on the initial conditions, releasing/absorbing water and CO_2 molecules to/from the aqueous solution, until the solution phase reaches the equilibrium condition. Although the final state is independent of the initial CO_2 concentration in the aqueous phase, care must be taken in finite systems as those studied in this work. Initial conditions must be close enough to coexistence so that the system is able to reach equilibrium before exhaustion of any of the phases at coexistence. In this particular work, we have checked that density profiles of water and CO_2 in the aqueous phase reach the equilibrium value. This is practically done monitoring the averages profiles every 100 ns until no significant variations in their bulk region are observed. Once densities of water and CO_2 are obtained, the molar fraction of CO_2 in the aqueous solution is calculated from the corresponding averaged density values.

We use simulation boxes of solutions containing 4000 water molecules and varying the number of CO_2 molecules depending on temperature: 50 (250, 260, and 270 K), 120 (280 and 290 K), and 240 (295 K) CO_2 molecules. We equilibrate each simulation box during 40 ns using the isothermic–isobaric or $NP_z\mathscr{A}T$ ensemble. In this case, two of the dimensions of the simulation boxes, arbitrarily named L_x and L_y, are kept constant [$L_x = L_y$ vary between 4.77 and 4.82 nm ($\mathscr{A} \simeq 15 \times 15\,\sigma^2$) depending on the temperature] and equal to the values of two lengths of the simulation box of the hydrate. L_z is however allowed to vary to achieve the equilibrium pressure of 400 bar. Particularly, L_z varies from 10.28 to 10.53 nm depending on the temperature. Finally, the equilibrated hydrate and

Downloaded from http://pubs.aip.org/aip/jcp/article-pdf/doi/10.1063/5.0146618/17414902/184703_1_5.0146618.pdf

Published under an exclusive license by AIP Publishing

aqueous solution simulation boxes are assembled along the z direction sharing a planar solid–liquid interface with interfacial area $\mathcal{A} = L_x \times L_y$. We then perform simulations in the *NPT* ensemble using an anisotropic barostat with pressures identical in the three directions and equal to 400 bar. This allows the solid to relax and avoid any stress and obtain the correct value of the solubility at each temperature. Systems are equilibrated during 100 ns. After this, we run additional 300 ns to obtain the equilibrium density profiles of the system from 250 up to 295 K.

Figure 6 shows the density profiles of water and CO_2 molecules as obtained from anisotropic *NPT* simulations at 400 bar and temperatures ranging from 250 to 295 K. The density profiles have been obtained as explained in Sec. III A. Note that at temperatures above 295 K, it is not possible to determine the solubility because the hydrate melts. In other words, there is a kinetic limit at high temperatures to determine the solubility of CO_2 from the hydrate.

As in the case of the LL coexistence described in Sec. III A, we only plot half of the profiles corresponding to one of the interfaces exhibited by the system. The right side of Fig. 6 corresponds to the hydrate phase and the left side to the aqueous solution phase. The density profiles in the hydrate phase exhibit the usual solid-like behavior for water and CO_2 molecules, with peaks at the corresponding crystallographic equilibrium position at which molecules are located in the hydrate. As can be seen, the density profiles at the lowest temperatures from 250 up to 280 K show nearly the same structure, and only small differences are observed at the hydrate–solution interface, as it is expected.

It is also interesting to analyze the behavior of profiles of water and CO_2 in the aqueous phase. The density profiles near the interface show some structural order due to the presence of the hydrate phase. Note that the positional order of the molecules is more pronounced at low temperatures below $T \leq 280$ K. The bulk density of water (left side of Fig. 6) slightly decreases as the temperature is increased, especially close to temperatures at which the hydrate melts. It is interesting to mention that bulk density profiles vary with temperature in the opposite way that when the aqueous solution is in contact with the CO_2 liquid phase (see Fig. 2).

The bulk density of CO_2 (in the aqueous solution phase) increases as the temperature is increased. From the inspection of Fig. 6, it is clearly seen that the hydrate phase becomes less stable as the temperature approaches to 290–295 K. At lower temperatures, the hydrate–solution interface is located at $z \approx 5$ nm, approximately, with the hydrate phase showing 6–7 well-defined CO_2 layers. However, at 290 and 295 K, only 5–6 layers can be observed in the hydrate phase, with the interface located at $z \approx 6$ nm. In fact, as we have previously mentioned, it is not possible to keep stable the hydrate at temperatures above 295 K, which eventually melts at higher temperatures.

We have calculated, from the information obtained from the density profiles, the solubility of CO_2 in the aqueous solution when it is in contact with the hydrate. As can be seen in Fig. 7, the solubility of CO_2 increases as the temperature is raised. We have also included in Fig. 7 (inset) the same results obtained previously by us corresponding to the methane + water system.[29] It can be seen that our results are in agreement with the results of the solubility of methane. Contrary to what happens in the case of the methane hydrate, it is only possible to calculate the solubility up to a temperature of 295 K. This is just a few degrees (around five) above the values of the three point temperature T_3 of the CO_2 hydrate at this pressure (see Sec. III D). In the case of our previous work, the hydrate was kept in metastable equilibrium at about 35 K over the dissociation temperature of the methane hydrate (295 K).[29]

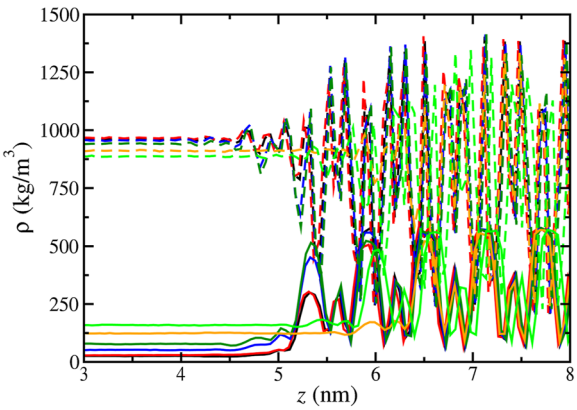

FIG. 6. Simulated equilibrium density profiles, $\rho(z)$, across the hydrate–CO_2 liquid interface of CO_2 (continuous curves) and water (dashed curves) as obtained from MD anisotropic *NPT* simulations at 400 bar and 250 (black), 260 (red), 270 (blue), 280 (dark green), 290 (orange), and 295 K (green).

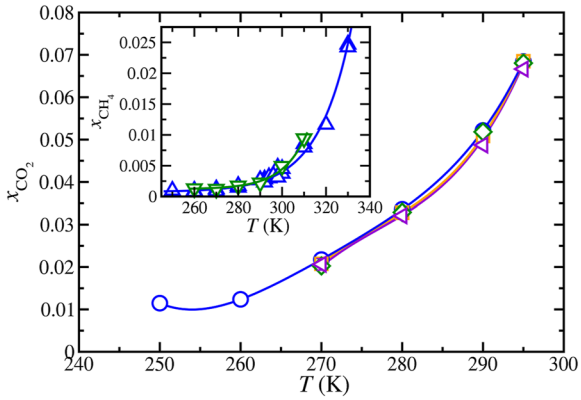

FIG. 7. Solubility of CO_2 in the aqueous phase, as a function of temperature, at 400 bar when the solution is in contact with the hydrate phase via a planar interface. The symbols correspond to solubility values obtained from MD anisotropic *NPT* simulations using cutoffs of 1.0 (blue circles) and 1.9 nm (dark green diamonds). Orange squares correspond to simulation results using a cutoff of 1.0 nm and long-range corrections. In all the previous cases, the hydrate is fully occupied by CO_2 molecules. Violet triangles left correspond to simulation results using a cutoff of 1.0 nm and an occupancy of 50% of the small or D cages (87.5% of overall occupancy). Inset: solubility of methane in water, as a function of temperature, at 400 bar when the solution is in contact with the hydrate phase via a planar interface. Solubility values of methane in water are taken from our previous work.[29] Simulations are performed at the same conditions using cutoffs of 0.9 nm (blue triangles up) and 1.7 nm (dark green triangles down). In all cases, the curves are included as guides to the eyes.

Downloaded from http://pubs.aip.org/aip/jcp/article-pdf/doi/10.1063/5.0146618/17414902/184703_1_5.0146618.pdf

Published under an exclusive license by AIP Publishing

We have also considered the impact of using different cutoff distances on solubilities. As in the case of the results presented in Sec. III A, we have used three different cutoff distances for the dispersive interactions. Particularly, we use the same two values, 1.0 and 1.9 nm. We have also performed simulations using standard long-range corrections to energy and pressure with a cutoff value of 1.0 nm. Contrary to what happens with the solubility of CO_2 in water when the solution is in contact with the other liquid phase (CO_2), the solubility does not depend on the cutoff distance, as can be seen in Fig. 7. Our results indicate that long-range corrections due to dispersive interactions have little or negligible effect on solubilities in aqueous solutions in contact with the hydrate. However, according to Figs. 3 and 5, long-range interactions play a key role in thermodynamic and interfacial properties in systems involving fluid phases.[69,70,77–80]

We have considered the effect of the CO_2 occupancy in the hydrate on the solubility in the aqueous solution. We have prepared initial simulation boxes in a similar way to the case of full occupancy but with CO_2 occupying half of the small or D cages. Particularly, we use 2944 water ($46 \times 4 \times 4$) and 448 CO_2 molecules. This means that the occupancy of the large or T cages is 100% (384 CO_2 molecules) and the occupancy of the small or D cages is 50% (64 CO_2 molecules). This represents a 87.5% of occupancy of D and T cages. According to the experimental data,[81–84] the equilibrium occupancy of large or T cages of the CO_2 hydrate is nearly 100%. However, although there is a large discrepancy in measurements and predictions of the small cage occupancy, it is generally accepted that the occupancy of small or D cages is ~30–60% depending on thermodynamic conditions. Note that with this occupancy (i.e., overall 87.5%), the ratio of water to CO_2 molecules in the hydrate is not 5.75 (as when the occupancy is 100%), but its value is now $46/7 \approx 6.57$. We follow the same procedure explained in the previous paragraph, with a cutoff distance of 1.0 nm. As a result, we obtain similar density profiles to those shown in Fig. 6. The solubility of CO_2 in water when the aqueous solution is in contact with the hydrate with 87.5% of occupancy is also shown in Fig. 7. As can be seen, the solubility of CO_2 when it is in contact with the hydrate with an occupancy of 87.5% is the same as that when it is in contact with the hydrate fully occupied within the error bars.

Finally, it is important to remark that, contrary to what we have found in our previous work for the solubility of methane in water,[29] we do not find a melting of the hydrate in a two-step process, i.e., a bubble of pure methane appears in the liquid phase as a first step and then the methane of the aqueous solution moves to the bubble and the methane from the hydrate moves to the aqueous solution as a second step. We find here that the hydrogen bonds of the layer of the hydrate in contact with the aqueous solutions break and the hydrate starts to melt. Particularly, when the temperature is increased, the concentration of CO_2 in the aqueous solution increases in order to stabilize the hydrate phase. In the case of the methane hydrate, the amount of methane molecules released to the aqueous phase to achieve the new equilibrium state is small (the solubility of methane in water is very small) and the metastable hydrate phase can exists above the T_3. However, in the case of the CO_2 hydrate, CO_2 saturates the aqueous phase (the solubility of CO_2 in water increases greatly with the temperature). The hydrate becomes unstable, the hydrogen bonds of the hydrate layer next to the aqueous solution break, and the hydrate finally melts.

D. Three-phases coexistence from solubility calculations

We have obtained the solubility of CO_2 in the aqueous solution, as a function of the temperature at a fixed pressure of 400 bar, when it is in contact with the CO_2 liquid phase (Sec. III A) and with the hydrate (Sec. III C). In both cases, the system exhibits two-phase coexistence. It is interesting to represent both solubilities in the same plot, as we did in our previous study[29] and as it is shown in Fig. 8. Since one of the solubility curves is a decreasing function of the temperature and the other is an increasing function of the temperature, there exists a certain temperature, which we will call T_3 for reasons that will be clear soon, at which both solubilities are equal at 400 bar.

The points of the solubility curve of CO_2 in the aqueous solution from the CO_2 liquid phase correspond to thermodynamic states at which the pressure and the chemical potentials of water and CO_2 in the aqueous phase are equal to those in the CO_2 liquid phase. In addition to this, the points of the solubility of CO_2 in water from the hydrate phase correspond to states at which the pressure is also the same and at which the chemical potentials of both components in the aqueous phase are equal to those in the hydrate phase. Consequently, at T_3, the temperature, pressure, and chemical potentials of water and CO_2 in the aqueous solution, CO_2 liquid, and hydrate phases are the same. This means that the point at which the two solubility curves cross represents a three-phase coexistence state of the system at 400 bar. This is also known as the dissociation temperature of the CO_2 hydrate at the corresponding pressure (400 bar).

The value obtained in this work for T_3 is 290(2) K when the occupancy of the hydrate is 100% (all the T and D cages are occupied by CO_2 molecules). We assume here an uncertainty of 2 K for

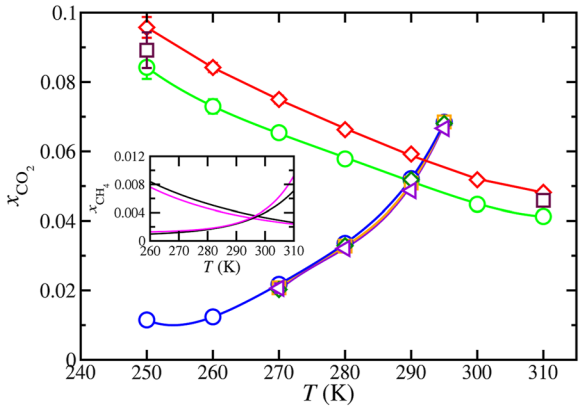

FIG. 8. Solubilities of CO_2 from the CO_2 liquid and the hydrate along the isobar $P = 400$ bar. The crossing of the two curves determines the dissociation temperature of the hydrate, T_3, at 400 bar. The symbols and colors are the same as those in Figs. 3 and 7. In all the previous cases, the hydrate is fully occupied by CO_2 molecules. Violet triangles left correspond to simulation results using a cutoff of 1.0 nm and an occupancy of 50% of the small or D cages (87.5% of overall occupancy). Inset: solubilities of methane from the gas and the hydrate phase, as a function of temperature, at 400 bar. Solubility values of methane in water are taken from our previous work.[29] Simulations are performed at the same conditions using cutoffs of 0.9 nm (black curves) and 1.7 nm (violet curves). In all cases, the curves are included as guides to the eyes.

Downloaded from http://pubs.aip.org/aip/jcp/article-pdf/doi/10.1063/5.0146618/17414902/184703_1_5.0146618.pdf

Published under an exclusive license by AIP Publishing

the dissociation temperature of the hydrate, following the same estimation of the T_3 error of the methane hydrate determined in our previous work.[29] We have also determined the dissociation temperature of the hydrate when the occupancy of the small or D cages is 50% (87.5% overall occupancy) using r_c = 1.0 nm. In this case, T_3 = 290(2) K, which is the same value obtained for the fully occupied hydrate within the error. Both dissociation temperature results seem to be occupancy-independent with the employed methodology and are in good agreement (within the corresponding uncertainties) with the value obtained by Míguez *et al.* using the direct coexistence technique,[22] 287(2) K. It is important to remark here that we are using the same models for water (TIP4P/Ice)[64] and CO_2 (TraPPE),[65] the same unlike dispersive interactions between both components, and cutoff distance for dispersive interactions (r_c = 1.0 nm) than in the work of Míguez *et al.*[22] At this point, it is important to remark that the system sizes of this work are different than that used in the work of Míguez *et al.*,[22] and this could have a subtle effect in T_3 because of finite-size effects, as it has been found for the melting point of ice Ih.[85] The experimental value of T_3 at 400 bar is 286 K so that the force field used in this work provides a quite reasonable prediction.

Other authors have determined T_3 for this system from computer simulation. Costandy *et al.*[51] calculated the dissociation temperature of the CO_2 hydrate at 400 bar using the direct coexistence technique. They obtained a value of 283.5(1.7) K. Although they also used the same water and CO_2 models, a number of differences lead to a slightly different value of T_3: different unlike dispersive interactions between water and CO_2 and cutoff distance for dispersive interaction (1.1 nm). Waage *et al.*[19] also determined the dissociation line of the hydrate using free energy calculations. They also used the same models for water and CO_2 but different unlike dispersive interactions between them. In this case, the cutoff distance for dispersive interactions is r_c = 1.0 nm. These authors calculated the dissociation temperature of the hydrate at 200 and 500 bar. The values obtained are 283.9(1.7) and 284.8(0.9) K, respectively. Interpolating to 400 bar, T_3 is 284.5 K, in good agreement with the results of Costandy *et al.*[51] Unfortunately, the result obtained here cannot be compared with the predictions of Costandy *et al.*[51] and Waage *et al.*[19] since dispersive interactions are not the same as those used here.

Finally, it is important to focus on the effect of the cutoff distance used to evaluate long-range dispersive interactions. The T_3 value of 290(2) K has been obtained using a cutoff distance of 1.0 nm. We have also analyzed the solubilities of CO_2 from the CO_2 liquid and the hydrate phases using a much larger cutoff distance (i.e., 1.9 nm). As we have previously shown, the solubility of CO_2 from the CO_2 liquid phase increases when the value of the cutoff is increased. On the other hand, the solubility of CO_2 in the hydrate phase is not affected by the use of larger cutoff values. Consequently, the combined effect of the increase of the cutoff distance of the dispersive interactions is an increase of the T_3 since it is the intersection of the two solubility curves shown in Fig. 8. Particularly, the dissociation temperature of the hydrate is now found at 292(2) K, 2 K above T_3 observed with a cutoff distance of 1.0 nm, approximately.

It is interesting to compare the effect of the cutoff due to the dispersive interaction in both CO_2 and methane hydrates. As can be seen, in the case of the methane hydrate, T_3 is shifted toward lower temperatures, by 2 K, when the cutoff is increased. In the current case (CO_2 hydrate), we observed the opposite effect, i.e., T_3 increases when the cutoff distance is increased. This is the same effect as observed for the solubility curve of CO_2 in the aqueous solution in contact with the CO_2 liquid phase. This effect, contrary to that observed in the methane hydrate, could be due to the electrostatic interactions of the quadrupole of CO_2 with other CO_2 molecules and also with water molecules, which is not present in the case of the methane. We think that this issue deserves a more detailed study, but this is out of the scope of the current work.

We have determined the dissociation line of the CO_2 hydrate at 400 bar from the calculation of the solubility of CO_2 when the aqueous solution is in contact with the other two phases in equilibrium, the CO_2 liquid phase and the hydrate phase. Grabowska *et al.*[29] already demonstrated that this route allows to determine T_3 of hydrates. This work confirms that this methodology is a good alternative to the direct coexistence method. Particularly, it shows a slightly better efficiency compared with the other technique (lesser simulation times are required) and provides consistent values of T_3.

E. Driving force for nucleation of hydrates

The dissociation line of the CO_2 hydrate separates its phase diagram in two parts in which two different two-phase coexistence regions exist.[4] At a certain pressure, for instance, 400 bar, at temperatures above T_3, the system exhibits LL immiscibility between an aqueous solution and a CO_2 liquid phase. Note that the solubility of water in CO_2 is very small and the CO_2 liquid phase can be considered pure CO_2, in practice. However, at temperatures below T_3, the system exhibits SL phase equilibrium between the hydrate and a fluid phase (water or CO_2 depending on the global composition of the system). This is consistent with the nature of the dissociation or three-phase line at which the hydrate, aqueous solution, and CO_2 liquid phases coexist.

The fluid phase in equilibrium with the hydrate below T_3 depends on the global composition of the system. Here, we assume that the hydrate is fully occupied by CO_2 molecules, i.e., eight CO_2 molecules for every 46 water molecules according to the stoichiometry of hydrates type sI. Let N_{H_2O} and N_{CO_2} be the number of water and CO_2 molecules used in the fluid phases during the simulations, respectively. If the ratio $N_{H_2O}/N_{CO_2} > 5.75$, one should have hydrate–water phase separation (below T_3). However, if $N_{H_2O}/N_{CO_2} < 5.75$, one should have a hydrate–CO_2 phase system for $T < T_3$.

As described by Kashchiev and Firoozabadi[53] and Grabowska *et al.*,[29] the formation of a hydrate in the aqueous solution phase can be viewed as a chemical reaction that takes place at constant P and T,

$$CO_2(\,\mathrm{aq}, x_{CO_2}) + 5.75\,H_2O(\,\mathrm{aq}, x_{CO_2}) \rightarrow [CO_2(H_2O)_{5.75}]_H. \quad (7)$$

Since we work at constant pressure in this work (P = 400 bar), we drop the dependence of P in the rest of equations. Assuming that all the cages of the hydrate are filled, a unit cell of CO_2 hydrate is formed by 46 water molecules and eight CO_2 molecules, i.e., 1 CO_2 molecule per 46/8 = 5.75 water molecules. According to this, Eq. (7) considers the hydrate as a new compound formed from one molecule of CO_2 and 5.75 molecules of water. We can also associate

Downloaded from http://pubs.aip.org/aip/jcp/article-pdf/doi/10.1063/5.0146618/17414902/184703_1_5.0146618.pdf

Published under an exclusive license by AIP Publishing

with this compound one unique chemical potential for the hydrate at T, $\mu_H^H(T)$. Note that this chemical potential is simply the sum of the chemical potential of CO_2 in the solid plus 5.75 times the chemical potential of water in the solid, i.e.,

$$\mu_H^H(T) = \mu_{CO_2}^H(T) + 5.75\,\mu_{H_2O}^H(T). \tag{8}$$

According to the previous discussion, the compound $[CO_2(H_2O)_{5.75}]_H$ is simply the "hydrate" and we call one "molecule" of the hydrate in the solid the molecule $[CO_2(H_2O)_{5.75}]$.

Following the work of Kashchiev and Firoozabadi,[53] we denote the driving force for nucleation of the hydrate formed from the aqueous solution with a concentration x_{CO_2} at T as

$$\Delta\mu_N(T, x_{CO_2}) = \mu_H^H(T) - \mu_{CO_2}^{aq}(T, x_{CO_2}) - 5.75\,\mu_{H_2O}^{aq}(T, x_{CO_2}). \tag{9}$$

Note that $\Delta\mu_N$ in this paper is $\Delta\mu_{nucleation}$ in our previous paper.[29] $\Delta\mu_N$ also depends on pressure, but since we are working at constant pressure (400 bar), we drop the pressure dependence from all the equations in this study. $\mu_H^H(T)$ has been previously defined in Eq. (8) as the chemical potential of the "hydrate molecule" in the hydrate phase, and $\mu_{CO_2}^{aq}(T, x_{CO_2})$ and $\mu_{H_2O}^{aq}(T, x_{CO_2})$ are the chemical potentials of CO_2 and water in the aqueous solution, respectively, at T and molar fraction of CO_2, x_{CO_2}. Note that the composition of CO_2 in Eq. (9) is *a priori*, independent of the pressure and temperature selected. In other words, one could have different driving forces for nucleation, at a given P and T, changing the composition of the aqueous solution (for instance, in a supersaturated solution of CO_2). However, there exists a particular value of x_{CO_2}, which is of great interest from the experimental point of view. Experiments on the nucleation of hydrates are performed when the water phase is in contact with the CO_2 liquid phase through a planar interface. Since both phases are in equilibrium at P and T, the solubility of CO_2 in water (molar fraction of CO_2 in the aqueous solution) is fully determined since $x_{CO_2}^{eq} \equiv x_{CO_2}^{eq}(T)$. Following the notation of Grabowska *et al.*,[29] the driving force for nucleation at experimental conditions is given by

$$\Delta\mu_N^{EC}(T) = \mu_H^H(T) - \mu_{CO_2}^{aq}(T, x_{CO_2}^{eq}(T)) - 5.75\,\mu_{H_2O}^{aq}(T, x_{CO_2}^{eq}(T)). \tag{10}$$

Note that $\Delta\mu_N^{EC}$ depends only on T (and on P, but in this work, we are working at the same P = 400 bar). We provide here valuable information for this magnitude when the molecules are described using the TIP4P/Ice and TraPPE models for water and CO_2, respectively.

In Secs. III E 1–III E 5, we concentrate on the driving force for nucleation at experimental conditions, $\Delta\mu_N^{EC}(T)$, obtained using four different routes. In the first one (route 1), we use the definition of the driving force of nucleation given by Eq. (10). In the second one (route 2), we use the solubility curves of CO_2 from the hydrate and the CO_2 liquid phase. In third one (route 3), we use the enthalpy of dissociation of the hydrate and assume that it does not change with temperature nor composition. In the fourth one (route 4), we propose a novel methodology based on the use of the solubility curve of CO_2 with the hydrate, valid not only for the CO_2 hydrate but also for other hydrates. This route can be used to determine $\Delta\mu_N$ at any arbitrary temperature and mixture composition and not only at experimental conditions. Finally, we discuss the results obtained using the different routes and compare the driving force for nucleation of the CO_2 hydrate with that of the methane hydrate previously obtained by us in a previous study.[30]

1. Route 1 for calculating $\Delta\mu_N^{EC}$

Route 1 was proposed and described in our previous work,[29] and we summarize here only the main approximations and the final expression of the driving force for nucleation. To evaluate $\Delta\mu_N^{EC}(T, x_{CO_2}^{eq})$ in Eq. (10), we need to calculate the chemical potential of the "hydrate molecule" in the hydrate phase and the chemical potentials of CO_2 and water in the aqueous phase at a supercooled temperature T below T_3. The change in the hydrate chemical potential when the temperature passes from T_3 to T can be evaluated in a similar way as that for pure CO_2 from T_3 to T. In fact, this later change has been already calculated in Sec. III A using Eq. (5) and evaluated from the corresponding thermodynamic integration using computer simulations in the *NPT* ensemble.

The chemical potential of water in the aqueous phase at T can be estimated using the procedure of Grabowska *et al.*[29] applied to the case of the CO_2 hydrate according to Eqs. (20)–(26) of their paper. This is done in two steps. In the first step, the change in the chemical potential of the solution when its temperature passes from T_3 to T is approximated by that of pure water calculated from thermodynamic integration [see Eqs. (24) and (26) of the work of Grabowska *et al.*[29]]. The second step involves the change in the chemical potential of water in the solution when the composition of CO_2 changes from $x_{CO_2}^{eq}(T_3)$ to $x_{CO_2}^{eq}(T)$ [see Eq. (25) of our previous work]. The rigorous calculation of this contribution requires the knowledge of the activity coefficient of water in an aqueous solution with a given composition of water, $\gamma_{H_2O}^{aq}(T, x_{H_2O}^{eq})$, at T and T_3. Grabowska *et al.* assumed that this magnitude, in the case of an aqueous solution of methane, $\gamma_{H_2O}^{aq} \approx 1$ since the solution is very diluted. We follow here the same assumption.

Using these approximations, it is possible to compute the driving force at experimental conditions for nucleation given by Eq. (10). The final expression is given by

$$\frac{\Delta\mu_N^{EC}(T, x_{CO_2}^{eq})}{k_BT} = -\int_{T_3}^{T} \frac{h_H^H(T') - \{h_{CO_2}^{pure}(T') + 5.75 h_{H_2O}^{pure}(T')\}}{k_BT'^2}\,dT' - \left[k_BT\,\ln\{x_{H_2O}^{eq}(T)\} - k_BT_3\,\ln\{x_{H_2O}^{eq}(T_3)\}\right]. \tag{11}$$

Here, $h_H^H = H/N_{CO_2}$ is the enthalpy H of the hydrate per CO_2 molecule and N_{CO_2} is the number of CO_2 molecules in the hydrate. Note that Eq. (11) is consistent with the view of Kashchiev and Firoozabadi[53] of the hydrate as a new compound formed from one molecule of CO_2 and 5.75 molecules of water when the hydrate is fully occupied. In addition, note that it is necessary to use that the driving force for nucleation at T_3 is equal to zero, i.e.,

$$\Delta\mu_N^{EC}(T_3, x_{CO_2}^{eq}) = \mu_H^H(T_3) - \mu_{CO_2}^{aq}(T_3, x_{CO_2}^{eq}(T_3)) - 5.75\,\mu_{H_2O}^{aq}(T_3, x_{CO_2}^{eq}(T_3)) = 0. \tag{12}$$

This is equivalent to arbitrarily setting to zero the chemical potentials of CO_2 and water in the hydrate at T_3. Equation (11) is similar to Eq. (15) (route 3 or dissociation route) but taking into account two effects: (1) the temperature dependence of molar enthalpies of hydrate, CO_2, and water and (2) the change of composition of the

Downloaded from http://pubs.aip.org/aip/jcp/article-pdf/doi/10.1063/5.0146618/17414902/184703_1_5.0146618.pdf

Published under an exclusive license by AIP Publishing

solution when passing from T_3 to T (see route 3 below for further details).

As previously mentioned, each change in the chemical potentials needed to compute the driving force for nucleation is obtained by evaluating molar enthalpies of pure CO_2, water, and hydrate phases involved in the integrals given by Eq. (11). Note that the chemical potential of CO_2 in the aqueous solution has been already obtained in Sec. III A. Particularly, since in this route one is interested in computing $\Delta\mu_N$ at experimental conditions, the chemical potential of CO_2 in the aqueous solution is equal to that of pure CO_2 at the same P and T. Consequently, it has been obtained from the integration of the molar enthalpy at several temperatures according to Eq. (5).

In the case of water, the chemical potential can be obtained performing MD *NPT* simulations of pure water along the 400 bar isobar. As in the case of pure CO_2, we also use the standard *NPT* in such a way that the three dimensions of the simulation box are allowed to fluctuate isotropically. We used a cubic simulation box with 1000 H_2O molecules. The dimensions of the simulation box L_x, L_y, and L_z vary depending on the temperature from 3.14 to 3.08 nm. Simulations to calculate the molar enthalpy, at each temperature, are run during 100 ns, 20 ns to equilibrate the system and 80 ns as the production period to obtain $h^{\text{pure}}_{H_2O}$.

In the case of the pure hydrate, we have obtained the chemical potential in a similar way, performing simulations in the *NPT* ensemble using an isotropic barostat at 400 bar. At the beginning of each simulation, we use a cubic box formed by 27 replicas of the unit cell in a $3 \times 3 \times 3$ geometry. The dimensions of the simulation box vary between 3.85 and 3.62 nm depending on the temperature. As in the rest of simulations, we calculate the enthalpy at different temperatures, from 260 to 295 K. Simulations are run during 100 ns, 20 ns to equilibrate the system and 80 ns to calculate the molar enthalpy of the hydrate.

2. Route 2 for calculating $\Delta\mu_N^{EC}$

Route 2 was also proposed and described in our previous work.[29] This route is inspired by the work of Molinero *et al.*,[31] and we summarize here only the main approximations and the final expression of the driving force for nucleation. According to this, it is possible to find a different, but an equivalent, thermodynamic route to calculate the driving force for the nucleation of methane hydrates. We check in this work whether this approach can also be used to deal with CO_2 hydrates. Let us consider Eq. (10) at experimental conditions, i.e., at the equilibrium composition of CO_2 in the aqueous solution when it is in contact via a planar interface with a CO_2 liquid phase (L), $x^{\text{eq}}_{CO_2}(T|\text{L})$. Note that the vertical line represents flat interface equilibrium with the liquid CO_2. To clarify the derivation of the final expression, we write explicitly the solubility of water in the solution, at experimental conditions, as $x^{\text{eq}}_{H_2O}(T|\text{L})$. Obviously, as we have previously mentioned in Sec. III A, the solubility of water in the solution can be obtained readily as $x^{\text{eq}}_{H_2O}(T|\text{L}) = 1 - x^{\text{eq}}_{CO_2}(T|\text{L})$.

We now assume that the chemical potential of the ideal solution's components can be expressed, in general, in terms of chemical potentials of pure components in the standard state and their molar fractions. In other words, since the molar fraction of CO_2 in the solution is small, we are assuming that water is the dominant component (solvent) and CO_2 is the minor component (solute) in the mixture. Under these circumstances, the activity coefficients of water and CO_2 are close to one.[86] According to this and following our previous work,[29] Eq. (10) can be written as

$$\Delta\mu_N^{\text{EC}}(T) = -k_BT\ln\left[\frac{x^{\text{eq}}_{CO_2}(T|\text{L})}{x^{\text{eq}}_{CO_2}(T|\text{H})}\right] - 5.75k_BT\ln\left[\frac{x^{\text{eq}}_{H_2O}(T|\text{L})}{x^{\text{eq}}_{H_2O}(T|\text{H})}\right], \tag{13}$$

where $x^{\text{eq}}_{CO_2}(T|\text{H})$ and $x^{\text{eq}}_{H_2O}(T|\text{H})$ represent the molar fraction of CO_2 and H_2O in the solution when it is in equilibrium via a planar interface (vertical line) with the hydrate phase (H), respectively. Note that $\Delta\mu_N^{\text{EC}}(T)$ and all the molar fractions also depend on pressure, but in this work, we work at fixed $P = 400$ bar. This is the equation obtained previously by us considering the driving force for the nucleation of the methane hydrate.[29] As we will see later in this section, Eq. (13) does not provide reliable values for the driving force of nucleation of the CO_2 hydrate, contrary to what happens with the methane hydrate. The solubilities of methane in the solution when is in contact with the methane phase and with the hydrate are one order of magnitude lower than those of CO_2 in the case of the CO_2 hydrate. Consequently, this route can be useful only in cases in which the solubility of the guest is extremely low.

3. Route 3 (dissociation) for calculating $\Delta\mu_N^{EC}$

It is possible to estimate the driving force for nucleation of a hydrate using a simple and approximate route based on the knowledge of the enthalpy of dissociation of the hydrate.[53] The dissociation enthalpy of the hydrate, $h^{\text{diss}}_{\text{H}}$, is defined as the enthalpy change of the process,[29]

$$[CO_2(H_2O)_{5.75}]_{\text{H}} \rightarrow CO_2(\text{liq}) + 5.75\,H_2O(\text{liq}). \tag{14}$$

Dissociation enthalpies are usually calculated assuming that the hydrate dissociates into pure water and pure CO_2. Note that this corresponds to the definition of enthalpy of dissociation and that in reality CO_2 will be dissolved in water and an even smaller amount of water will be dissolved in the CO_2 liquid phase. We have determined the dissociation enthalpy of the hydrate simply by performing simulations of the pure phases (hydrate, water, and CO_2) at several temperatures at 400 bar.

According to our previous work,[29] we evaluate the driving force for nucleation assuming the following approximations: (1) the enthalpy of dissociation of the hydrate $h^{\text{diss}}_{\text{H}}$ does not change with the temperature, (2) its value can be taken from $h^{\text{diss}}_{\text{H}}(T_3)$, and (3) enthalpy of dissociation does not vary with composition of the aqueous solution containing CO_2 when the temperature is changed. According to this, $\Delta\mu_N^{\text{EC}}$ is given by

$$\Delta\mu_N^{\text{EC}} = k_BT\int_{T_3}^{T}\frac{h^{\text{diss}}_{\text{H}}}{k_BT'^2}\,dT' \cong -h^{\text{diss}}_{\text{H}}(T_3)\left(1-\frac{T}{T_3}\right). \tag{15}$$

Note that Eq. (11) reduces to Eq. (15) under the approximations used in this route.

4. Route 4 for calculating $\Delta\mu_N^{EC}$

The driving force for the nucleation of the CO_2 hydrate, at any arbitrary temperature, T_N, and molar fraction of CO_2 in the aqueous solution, $x^{(\text{N})}_{CO_2}$, at fixed pressure is defined as

$$\Delta\mu_{\text{N}}(T_{\text{N}}, x^{\text{N}}_{CO_2}) = \mu^{\text{H}}_{\text{H}}(T_{\text{N}}) - \mu^{\text{aq}}_{CO_2}(T_{\text{N}}, x^{\text{N}}_{CO_2}) - 5.75\,\mu^{\text{aq}}_{H_2O}(T_{\text{N}}, x^{\text{N}}_{CO_2}). \tag{16}$$

Downloaded from http://pubs.aip.org/aip/jcp/article-pdf/doi/10.1063/5.0146618/17414902/184703_1_5.0146618.pdf

Published under an exclusive license by AIP Publishing

Note that $\Delta\mu_N$ also depends on pressure. However, since we work at constant pressure ($P = 400$ bar), we drop the pressure dependence from equations from this point. It is also important to recall that since we are assuming that all cages of the hydrate are filled, the chemical potential of a "hydrate molecule" in the hydrate phase depends only on temperature. Finally, the chemical potentials of CO_2 and water also depend on the molar fraction of water in the aqueous solution, $x^N_{H_2O}$. Since we are dealing with a binary mixture, $x^N_{H_2O} = 1 - x^N_{CO_2}$. For simplicity, we choose $x^N_{CO_2}$ as an independent variable of the chemical potentials of CO_2 and water in the solution.

The driving force for nucleation of the CO_2 hydrate, $\Delta\mu_N$, depends on T_N and $x^N_{CO_2}$, and both are independent variables. This means that route 4 is valid for calculating the driving force for nucleation at any T_N and $x^N_{CO_2}$. As we will see later, the method can be particularized to evaluate $\Delta\mu_N$ at experimental conditions. In this case, $\Delta\mu_N = \Delta\mu^{EC}_N(T_N) = \Delta\mu^{EC}_N(T_N, x^{eq}_{CO_2}(T_N|\,L))$, as we have previously mentioned.

To evaluate $\Delta\mu_N$, we need to calculate the chemical potential of the "hydrate molecule," $\mu^H_H(T_N)$, at a supercooled temperature T_N and the chemical potentials of CO_2 and water molecules of an aqueous solution of CO_2 with molar fraction $x^N_{CO_2}$ at the same temperature. This route is based on the use of the solubility curve of the hydrate with temperature, at constant pressure, previously described in Sec. III C. A schematic depiction of the curve and the thermodynamic route for obtaining $\Delta\mu_N$ at arbitrary T_N and $x^N_{CO_2}$ is represented in Fig. 9. Let us consider a reference state in our calculations at temperature T_{ref} on the solubility curve in contact with the hydrate. As it will be clear later, the particular value of T_{ref} is not important since we are dealing with differences of chemical potentials and the final value of $\Delta\mu_N$ does not depend on the election of the reference state. Due to this, the reference state does not appear in Fig. 9.

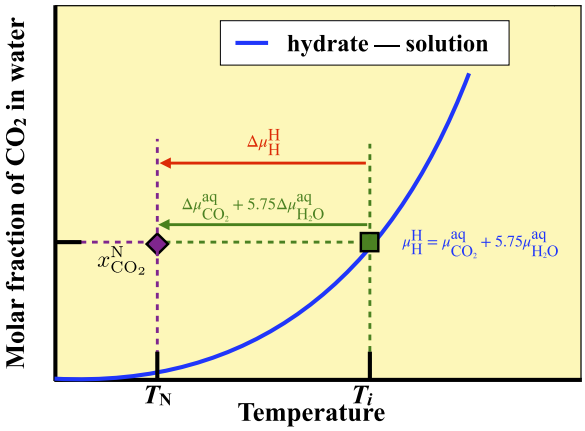

FIG. 9. Schematic depiction of route 4 for obtaining $\Delta\mu_N$. The blue solid curve represents the solubility curve of CO_2 with the hydrate (hydrate–solution equilibrium). The green square is a state at T_i at which the aqueous solution with molar fraction $x^N_{CO_2}$ is in equilibrium with the hydrate phase, and the magenta diamond is the state at T_N and $x^N_{CO_2}$ at which $\Delta\mu_N$ is calculated. The arrows in colors represent the paths followed by thermodynamic integration, from T_i to T_N, of the molar enthalpy of the "hydrate molecule" (red arrow) and the partial molar enthalpies of CO_2 and water (green arrow) using Eq. (26).

The first contribution to $\Delta\mu_N$ in Eq. (16) is the chemical potential of the "hydrate molecule" in the hydrate phase at T_N. The chemical potential μ^H_H can be obtained using the Gibbs–Helmholtz thermodynamic relation for pure systems,

$$\left(\frac{\partial(\mu^H_H/T)}{\partial T}\right)_{P,N_H} = -\frac{h^H_H}{T^2}, \tag{17}$$

where $h^H_H = h^H_H(T)$ is the molar enthalpy of the "hydrate molecule" and the derivative is performed at constant pressure, P, and number of "hydrate molecules," N_H. Note that here h^H_H represents the enthalpy of the hydrate per molecule of CO_2 according to the definition in Sec. III E 1. The chemical potential of the "hydrate molecule" in the hydrate phase at a supercooling temperature T_N can be obtained by integrating Eq. (17) from T_{ref} to T_N as

$$\frac{\mu^H_H(T_N)}{k_B T_N} = \frac{\mu^H_H(T_{ref})}{k_B T_{ref}} - \int_{T_{ref}}^{T_N} \frac{h^H_H(T)}{k_B T^2}\, dT. \tag{18}$$

The last two contributions to the driving force for nucleation in Eq. (16), $\mu^{aq}_{CO_2}$ and $\mu^{aq}_{H_2O}$, need to be evaluated at temperature T_N and molar fraction $x^N_{CO_2}$. Individual chemical potentials of CO_2 and water in the solution at a given temperature are not easy to evaluate, as we have seen in routes 1 and 2. However, it is possible to use the solubility curve of CO_2 with the hydrate to overcome this problem.

Let T_i be the temperature at which the aqueous solution with molar fraction $x^N_{CO_2}$ is in equilibrium with the hydrate phase, as indicated in Fig. 9. Since both phases are in equilibrium at these conditions, the chemical potentials of CO_2 and water in the hydrate phase and in the aqueous solution are equal,

$$\mu^H_{CO_2}(T_i) = \mu^{aq}_{CO_2}(T_i, x^N_{CO_2}), \tag{19}$$

$$\mu^H_{H_2O}(T_i) = \mu^{aq}_{H_2O}(T_i, x^N_{CO_2}). \tag{20}$$

Note that $x^N_{CO_2} = x^{eq}_{CO_2}(T_i|\,H)$ according to the nomenclature used in Sec. III E 2 (route 2) and in our previous paper.[29] The vertical line here represents that the aqueous solution is in equilibrium with the solid hydrate via a flat interface.

Combining Eqs. (19) and (20) with Eq. (8), which gives the chemical potential of the "hydrate molecule" in terms of the chemical potentials of CO_2 and water in the hydrate phase, we obtain

$$\mu^H_H(T_i) = \mu^{aq}_{CO_2}(T_i, x^N_{CO_2}) + 5.75\,\mu^{aq}_{H_2O}(T_i, x^N_{CO_2}). \tag{21}$$

Equation (21) is the heart of route 4. According to it, the combination $\mu^{aq}_{CO_2} + 5.75\,\mu^{aq}_{H_2O}$ is known along the solubility curve of the hydrate at any temperature T_i: it is equal to the chemical potential of the "hydrate molecule" at the temperature considered. This apparently simple result allows us to calculate accurately the driving force for nucleation at any temperature and composition of the solution using a one-step thermodynamic integration. As it will be clear at the end of this section, this method can be used to determine the driving force for nucleation of other hydrates.

In the first step, we calculate the difference of $\mu^{aq}_{CO_2} + 5.75\,\mu^{aq}_{H_2O}$ between the reference state (ref) at T_{ref} and a second state (i) at T_i

Downloaded from http://pubs.aip.org/aip/jcp/article-pdf/doi/10.1063/5.0146618/17414902/184703_1_5.0146618.pdf

Published under an exclusive license by AIP Publishing

both on the solubility curve of CO_2 with the hydrate, as indicated in Fig. 9. According to Eq. (21), this is completely equivalent to evaluate the difference of μ_H^H between T_{ref} and T_i along the solubility curve. This change can be evaluated using again Eq. (17) (Gibbs–Helmholtz relation) and integrating between the two temperatures,

$$\frac{\mu_H^H(T_i)}{k_B T_i} = \frac{\mu_H^H(T_{ref})}{k_B T_{ref}} - \int_{T_{ref}}^{T_i} \frac{h_H^H(T)}{k_B T^2}\, dT. \tag{22}$$

In the second step, which involves the difference between the chemical potentials of CO_2 and water in solution at temperatures T_i and T at constant molar fraction, $x_{CO_2}^N$, $\Delta\mu_{CO_2}^{aq}$ and $\Delta\mu_{H_2O}^{aq}$, can be obtained from the Gibbs–Helmholtz equation for CO_2 and water,

$$\left(\frac{\partial(\mu_\alpha^{aq}/T)}{\partial T}\right)_{P,x_\alpha} = -\frac{\bar{h}_\alpha^{aq}}{T^2}. \tag{23}$$

Here, $\alpha = \{CO_2, H_2O\}$ and represents one of the components of the mixture. Note that the partial derivative is calculated at constant composition. In this case, the composition corresponds to that of the aqueous solution in equilibrium with the hydrate phase at T_i. $\bar{h}_\alpha^{aq}$ is the partial molar enthalpy of component α in the aqueous solution. The partial molar enthalpy is defined as

$$\bar{h}_\alpha^{aq} = N_A\left(\frac{\partial H}{\partial N_\alpha}\right)_{P,T,N_{\beta\neq\alpha}} = \lim_{\Delta N_\alpha\to 0} N_A\left(\frac{\Delta H}{\Delta N_\alpha}\right)_{P,T,N_{\beta\neq\alpha}}, \tag{24}$$

where N_A is Avogadro's number and H is the aqueous solution's enthalpy. The limit can be numerically evaluated computing the enthalpy for two systems that have the same number of water molecules and different number of CO_2 to evaluate the partial molar enthalpy of CO_2. The partial molar enthalpy of water can be estimated in a similar way, i.e., the number of molecules of CO_2 in the system is kept constant, while the number of water molecules changes. According to this, it is possible to evaluate the variation of the chemical potential of CO_2 and water from T_i to T_N, $\Delta\mu_{CO_2}^{aq}$ and $\Delta\mu_{H_2O}^{aq}$, from the knowledge of partial molar enthalpies of both components. In particular, the combination of the chemical potentials of CO_2 and water, as a function of T_N, can be obtained by integrating Eq. (23) as

$$\begin{aligned}\frac{\mu_{CO_2}^{aq}(T_N, x_{CO_2}^N) + 5.75\mu_{H_2O}^{aq}(T_N, x_{CO_2}^N)}{k_B T_N} &= \frac{\mu_{CO_2}^{aq}(T_i, x_{CO_2}^N) + 5.75\mu_{H_2O}^{aq}(T_i, x_{CO_2}^N)}{k_B T_i} \\ &- \int_{T_i}^{T_N} \frac{\bar{h}_{CO_2}^{aq}(T, x_{CO_2}^N) + 5.75\bar{h}_{H_2O}^{aq}(T, x_{CO_2}^N)}{k_B T^2} dT.\end{aligned} \tag{25}$$

Now, it is possible to find a closed expression for evaluating $\Delta\mu_N$ at arbitrary T_N and $x_{CO_2}^N$ in terms of the enthalpies of the "hydrate," CO_2, and water molecules. Using Eqs. (18), (21), (22), and (25), the driving force for nucleation can be written as

$$\begin{aligned}\frac{\Delta\mu_N(T_N, x_{CO_2}^N)}{k_B T_N} &= -\int_{T_i}^{T_N} \frac{h_H^H(T) - \left\{\bar{h}_{CO_2}^{aq}(T, x_{CO_2}^N) + 5.75\bar{h}_{H_2O}^{aq}(T, x_{CO_2}^N)\right\}}{k_B T^2} dT.\end{aligned} \tag{26}$$

We recall here that h_H^H is the enthalpy of the "hydrate molecule" per molecule of CO_2. Since we are assuming that the hydrate is fully occupied, the factor that multiplies the partial molar enthalpy of water must be 46/8 = 5.75 to be consistent with the stoichiometry of the unit cell. It is important to remark two important aspects of this expression. As we have previously mentioned, $\Delta\mu_N$ does not depend on the reference state. Note that the two integrations of the molar enthalpy of the "hydrate molecule" between T_{ref} and T_N, given by Eq. (18), and between T_{ref} to T_i, given by Eq. (22), are now expressed as a single integration of the molar enthalpy of the "hydrate molecule" between T_i and T_N. In other words, since the driving force for nucleation does not depend on the reference state, the initial state of Eq. (26) is simply T_i. This is also related to another important fact: the driving force for nucleation of the hydrate is zero not only at T_3 but also along the whole solubility curve of the hydrate.

The second interesting aspect of Eq. (26) is that the integrand of the right term can be formally written as an enthalpy of dissociation of the hydrate that depends on T_N and $x_{CO_2}^N$. Under this perspective, Eq. (26) resembles Eq. (15) of route 3 since it has the same mathematical form.

Equation (26) is a rigorous and exact expression (within the statistical uncertainties of the simulation results) obtained only from thermodynamic arguments for calculating the driving force for nucleation of the CO_2 hydrate at any T_N and $x_{CO_2}^N$. Obviously, this route is general and can be used to calculate driving forces for nucleation of other hydrates from the knowledge of the solubility curve of the corresponding guest with the hydrate.

Let us now apply this route to the particular case of the CO_2 hydrate and evaluate $\Delta\mu_N^{EC}(T)$ at experimental conditions, i.e., with $x_{CO_2}^N \equiv x_{CO_2}^{eq}(T|L)$. Each of the chemical potential changes in Eqs. (10) or (16) can be obtained evaluating the molar enthalpy

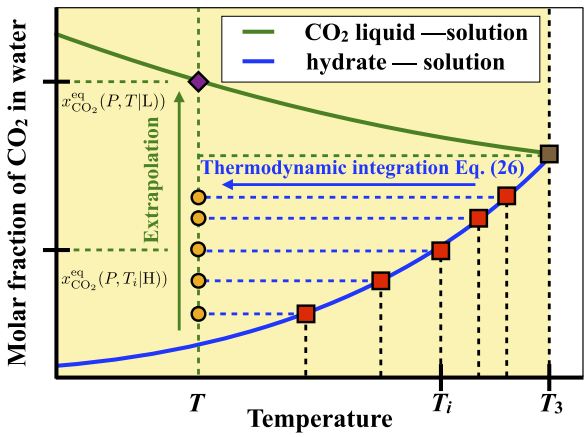

FIG. 10. Schematic depiction of route 4 for obtaining $\Delta\mu_N^{EC}$. Solid curves represent the solubility curves of CO_2 in water below T_3 for the CO_2 liquid–solution (green curve) and hydrate–solution (blue curve). The red squares represent hydrate–solution coexistence states at T_i and molar fractions $x_{CO_2}^{eq}(T_i|H)$. The dark yellow circles are states at a lower T and the same compositions. The magenta diamond is the CO_2 liquid–solution coexistence state obtained from extrapolation from states at T and molar fraction $x_{CO_2}^{eq}(T|L)$. $\Delta\mu_N^{EC}(T, x_{CO_2}(T|L))$ is obtained from extrapolation according to Figs. 13 or 14.

Downloaded from http://pubs.aip.org/aip/jcp/article-pdf/doi/10.1063/5.0146618/17414902/184703_1_5.0146618.pdf

Published under an exclusive license by AIP Publishing

of the "hydrate molecule" and the partial molar enthalpies of CO_2 and water in the aqueous solution in Eq. (26). In the case of the pure hydrate, the change in the chemical potential can be obtained performing simulations in the *NPT* ensemble using an isotropic barostat at 400 bar. At the beginning of each simulation, we use a cubic box formed by 27 replicas of the unit cell in a 3 × 3 × 3 geometry. The dimensions of the simulation box vary between 3.85 and 3.62 nm depending on the temperature. As in the rest of simulations, we calculate the enthalpy at different temperatures from 260 to 295 K. Simulations are run during 100 ns, 20 ns to equilibrate the system and 80 ns to calculate the molar enthalpy of the hydrate.

As can be seen in Fig. 8, the solubility curve of CO_2 with the liquid phase is a convex and decreasing function of temperature. According to this, it is not possible to reach this curve from the solubility curve of CO_2 with the hydrate from a temperature T_i below T_3 following the one-step thermodynamic path of route 4 (see also Fig. 9). A feasible solution is to choose a T_i value above T_3 where the hydrate–solution coexistence line is metastable. However, T_3 of the CO_2 hydrate is located at $T_3 = 290$ K [with molar fraction $x^{eq}_{CO_2}(T_3) = 0.05$], and the solubility curve with the hydrate can be only obtained up to 295 K, as shown in Fig. 7. This means that Eq. (26) can be only applied to calculate $\Delta\mu^{EC}_N$ for supercoolings above 270–280 K, approximately (depending on the value of the cutoff). In the case of the methane hydrate, it is possible to calculate the hydrate–solution equilibrium curve at temperatures significantly higher than T_3. This allows us to evaluate $\Delta\mu^{EC}_N$ at lower temperatures than in the case of the CO_2 hydrate (see the inset of Fig. 8 in this work and Fig. 4 of our previous work[29]).

To overcome this problem, we propose to use Eq. (26), for several values of $T_i < T_3$, and to perform an extrapolation of the composition at the temperature at which we evaluate $\Delta\mu^{EC}_N$, as indicated schematically in Fig. 10. According to this, $\mu^{aq}_{CO_2}$ and $\mu^{aq}_{H_2O}$, or the combination of both according to Eq. (25), can be obtained by performing *NPT* MD simulations of the solution along the 400 bar isobar at constant composition. As in the case of the "hydrate molecule," since we are simulating bulk phases, the standard *NPT* is used in such a way that the three dimensions of the simulation box are allowed to fluctuate isotropically. We evaluate the partial molar enthalpies of both components at five different concentrations: $x_{CO2} = 0.0680$, 0.0521, 0.0413, 0.0335, and 0.0215. These values are the compositions of the aqueous solution along the solubility curve of CO_2 with the hydrate, $x^{eq}_{CO_2}(T_i|\,H)$ at $T_i = 295$, 290, 285, 280, and 270, respectively. We calculate numerically the derivative of Eq. (24) by computing the enthalpy for two different systems that have the same number of water molecules and different numbers of CO_2 molecules and the same number of CO_2 molecules and different numbers of water molecules to determine $\bar{h}^{aq}_{CO_2}$ and $\bar{h}^{aq}_{H_2O}$, respectively. Particularly, $\bar{h}^{aq}_{H_2O}$ is obtained from the difference of the enthalpies of the aqueous solution using 990 and 1010 water molecules ($\Delta N_{H_2O} = 20$) for all the temperatures and compositions of the mixtures. In the case of $\bar{h}^{aq}_{CO_2}$, we have used different numbers of CO_2 molecules depending on the composition of the mixture: 20 and 24 ($\Delta N_{CO_2} = 4$) for $x_{CO2} = 0.0215$, 32 and 38 ($\Delta N_{CO_2} = 6$) for $x_{CO2} = 0.0335$, 40 and 46 ($\Delta N_{CO_2} = 6$) for $x_{CO2} = 0.0413$, 50 and 60 ($\Delta N_{CO_2} = 10$) for $x_{CO2} = 0.0521$, and 68 and 78 ($\Delta N_{CO_2} = 10$) for $x_{CO2} = 0.0680$. Simulations to calculate the enthalpy, at each temperature, are run during 300 ns, 50 ns to equilibrate the system and 250 ns as the production period. Dividing the enthalpy difference, ΔH, by the difference of the number of CO_2 molecules, ΔN_{CO_2}, and of the number of water molecules, ΔN_{H_2O}, and multiplying by Avogadro's constant, we get estimations of $\bar{h}^{aq}_{CO_2}$ and $\bar{h}^{aq}_{H_2O}$ at several compositions of the mixture and temperatures.

Figure 11 shows the partial molar enthalpy of CO_2 at five constant compositions as functions of the temperature. The composition of the mixture in each curve corresponds to the molar fraction of the solution at several temperatures, T_i, along the solubility curve of CO_2 with the hydrate, as indicated in the previous paragraph. The difference of the chemical potential of CO_2 along the integration path (see Fig. 9), $\Delta\mu^{aq}_{CO_2}$, is represented in the inset of Fig. 11. Note

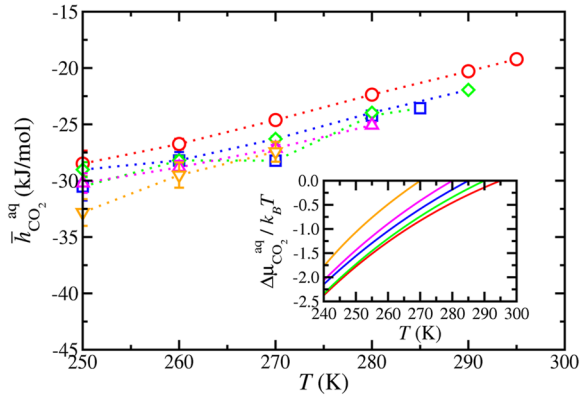

FIG. 11. Partial molar enthalpies of CO_2 in the aqueous solution, as a function of temperature, at different compositions: $x_{CO_2} = 0.0680$ (red circles), 0.0521 (green symbols), 0.0413 (blue symbols), 0.0335 (magenta triangles up), and 0.0215 (orange triangles down). In the inset, the difference of the chemical potential of CO_2, as a function of temperature, at the same compositions with respect to their values at the solubility curve of the hydrate at 295 (red), 290 (green), 285 (blue), 280 (magenta), and 270 K (orange) in shown. The vertical lines in the symbols represent the error bars. The dotted curves are guides to the eyes.

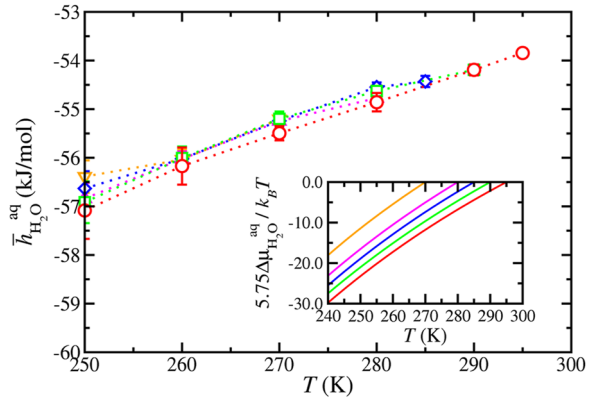

FIG. 12. Partial molar enthalpies of H_2O in the aqueous solution, as a function of temperature, at different compositions. In the inset, 5.75 times the difference of the chemical potential of H_2O, as a function of temperature, at the same compositions is shown. The symbols and colors are the same as those in Fig. 11. The vertical lines in the symbols represent the error bars. The dotted curves are guides to the eyes.

Downloaded from http://pubs.aip.org/aip/jcp/article-pdf/doi/10.1063/5.0146618/17414902/184703_1_5.0146618.pdf

Published under an exclusive license by AIP Publishing

that we have five different curves, one corresponding to each temperature value T_i. We follow the same approach and represent the partial molar enthalpy of water at the same compositions in Fig. 12. In the inset is now depicted $5.75\Delta\mu^{aq}_{H_2O}$, as a function of temperature, which represents the change of the rest of the "hydrate molecule" dissociated in the solution according to the nomenclature used in this section. As can be seen, partial molar enthalpies of CO_2 and water show small variations with the composition and decrease as the temperature decreases. The variation of both chemical potentials also exhibits similar behavior, i.e., they decrease as the temperature is lowered when keeping the composition of the mixture constant. In addition, each $\Delta\mu^{aq}_{CO_2} \to 0$ and $\Delta\mu^{aq}_{H_2O} \to 0$ at the temperature associated with the corresponding composition on the solubility curve of CO_2 with the hydrate.

Using the values of $\mu^{aq}_{CO_2}$ and $5.75\,\mu^{aq}_{H_2O}$, as functions of temperatures and at the molar fractions of CO_2 considered previously, it is possible to evaluate $\Delta\mu_N$ according to the scheme indicated in Fig. 10. Figure 13 shows $\Delta\mu_N$, as a function of x_{CO_2}, at four temperatures below T_3 (250, 260, 270, and 280 K). As can be seen, $\Delta\mu_N$ follows a linear dependence with the composition of the solution. We have performed linear regressions using the five values of x_{CO_2}, for each temperature, to obtain $\Delta\mu^{EC}_N$ at experimental conditions. We have also represented the compositions of the solution in equilibrium with the CO_2 liquid phase on the solubility curve of CO_2, $x^{eq}_{CO_2}(T|\,\mathrm{L})$ at the four temperatures (crosses and stars). As can be seen, we have two different values of $x^{eq}_{CO_2}(T|\,\mathrm{L})$ depending on the cutoff due to the dispersive interactions used, r_c = 1.0 (crosses) and 1.9 nm (stars).

It is also interesting to show $\mu^{aq}_{CO_2} + 5.75\,\mu^{aq}_{H_2O}$, as a function of composition, evaluated at several temperatures below T_3 of the hydrate, as shown in Fig. 14 (see also Fig. 10). Note that we have set to zero the chemical potentials of CO_2 and water in the hydrate at T_3 = 290 K. This representation contains the same information as Fig. 13 but allows us to discuss important aspects related to the approximations of route 3. We have represented $\mu^{aq}_{CO_2} + 5.75\,\mu^{aq}_{H_2O}$ at T = 250, 260, 270, and 280 K at the compositions $x^{eq}_{CO_2}$ previously selected (symbols). In addition to that, we have also represented the value of the change in the chemical potential of the hydrate, at the four temperatures, in equilibrium with the aqueous solution along the solubility curve of the hydrate. Note that the value of $\mu^{aq}_{CO_2} + 5.75\,\mu^{aq}_{H_2O}$ at 270 K is equal to that of the hydrate, $-11.2k_BT$, since it is in equilibrium with the solution with $x^{eq}_{CO_2}$ = 0.0215. The same is true at 280 K, i.e., $\mu^{aq}_{CO_2} + 5.75\,\mu^{aq}_{H_2O} = \mu^{H}_{H} = -5.4\,k_BT$, state at which the solution with x_{CO_2} = 0.0335 is in equilibrium with the hydrate.

The values of $\mu^{aq}_{CO_2} + 5.75\,\mu^{aq}_{H_2O}$, at the corresponding temperatures, follow a linear dependence with the composition of the solution. We have performed linear regressions using the five values obtained in this work, for each temperature, and the corresponding lines are also shown in Fig. 14. We have also represented the compositions of the solution in equilibrium with the CO_2 liquid phase on the solubility curve of CO_2, $x^{eq}_{CO_2}(T|\,\mathrm{L})$ at the four temperatures (crosses and stars). Note that these values fit in an excellent way to the linear regression. As can be seen, we have two different values of $x^{eq}_{CO_2}(T|\,\mathrm{L})$ depending on the cutoff due to the dispersive interactions used, r_c = 1.0 (crosses) and 1.9 nm (stars). See Fig. 8 and Sec. III D for further details. According to this, it is possible to know accurately the values of $\mu^{aq}_{CO_2} + 5.75\,\mu^{aq}_{H_2O}$ by extrapolating the linear fits depending on the temperature and the composition (see Fig. 13). These values, in combination with the values of $\mu^{H}_{H}(T)$ (already obtained in routes 1 and 2), can be used to predict with confidence the driving force for nucleation of the CO_2 hydrate using this new approach. Note that results obtained from Fig. 13 are the same than those obtained from Fig. 14 since they contain the same information.

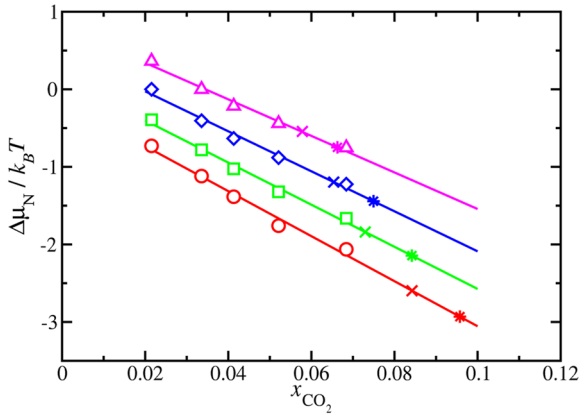

FIG. 13. $\Delta\mu_N$ values obtained from Eq. (26) according to route 4, as functions of composition, at 250 (red circles), 260 (green squares), 270 (blue diamonds), and 280 K (magenta triangles up). The continuous lines are linear regressions of $\Delta\mu_N$ values with x_{CO_2}, and the values of $\Delta\mu^{EC}_N$ at the molar fractions of the solution in equilibrium with the CO_2 liquid phase $x^{eq}_{CO_2}(T|\,\mathrm{L})$ using different cutoff distances r_c are represented by crosses (1.0 nm) and stars (1.9 nm).

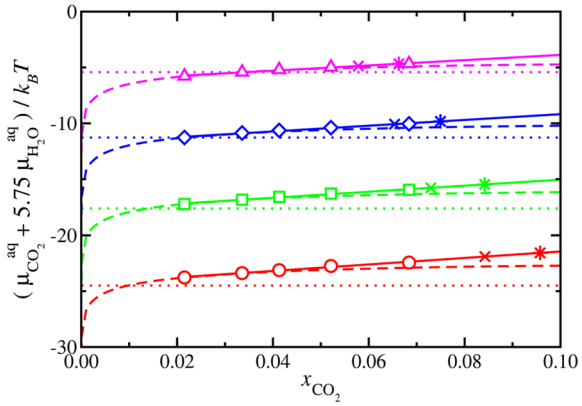

FIG. 14. $\mu^{aq}_{CO_2} + 5.75\,\mu^{aq}_{H_2O}$ values obtained from route 4, as functions of composition, at 250 (red circles), 260 (green squares), 270 (blue diamonds), and 280 K (magenta triangles up). The dotted horizontal lines represent the chemical potential values of the "hydrate molecules" in the hydrate phase, the continuous lines are linear regressions of the chemical potential values with x_{CO_2}, and the dashed curves are the chemical potential values at x_{CO_2} = 0.0215 and assuming a variation with the composition given by Eq. (13). The composition of the solution in equilibrium with the CO_2 liquid phase using different cutoff distances r_c is represented by crosses (1.0 nm) and stars (1.9 nm). We have set to zero the chemical potentials of CO_2 and water in the hydrate at T = 290 K.

Downloaded from http://pubs.aip.org/aip/jcp/article-pdf/doi/10.1063/5.0146618/17414902/184703_1_5.0146618.pdf

Published under an exclusive license by AIP Publishing

Before finishing this section, Fig. 14 contains valuable information that deserves to be discussed in detail. Dashed curves represent the values of $\mu^{aq}_{CO_2} + 5.75\,\mu^{aq}_{H_2O}$ obtained at the lowest concentration considered, $x_{CO2} = 0.0215$, and assuming that the variation with composition follows the approximation used in route 2 proposed by us in our previous work[29] and also used by Molinero *et al.*[31] and by us in this work. In other words, the difference of the chemical potentials of CO_2 and water when the composition is varied can be calculated, assuming that the activity coefficients of both components are close to 1 or are similar in the solution. Unfortunately, this approximation is not valid for CO_2 hydrates. As can be seen in Fig. 14, this approach (route 2) underestimates the value of $\mu^{aq}_{CO_2} + 5.75\,\mu^{aq}_{H_2O}$ more than $0.8k_BT$ (using $r_c = 1.0$ nm and more than $1k_BT$ using $r_c = 1.9$ nm) at 250 K with respect to the value obtained from route 4. As we will see later in Sec. III E 5, this result explains from a thermodynamic perspective why route 2 cannot be used with confidence to estimate the driving force for nucleation of the CO_2 hydrate.

5. Evaluation of $\Delta\mu_N^{EC}$ using different routes

We have obtained the driving force for nucleation of the CO_2 hydrate using the four routes presented in Secs. III E 1–III E 4. All the results have been obtained using a cutoff distance for the dispersive interactions $r_c = 1.0$ nm. As we have seen in the previous sections, this value of r_c gives a dissociation temperature of the hydrate $T_3 = 290(2)$ K. The results obtained using the different routes are represented in Fig. 15. Route 1 given by Eq. (11) predicts an almost linear behavior of $\Delta\mu^{EC}_N$ with the temperature. These results are in agreement with our previous results obtained for the driving force for nucleation of the methane hydrate.[29]

We have also used the novel route proposed in this work (route 4) based on the use of the solubility curve of CO_2 with the hydrate, given by Eq. (26). As mentioned in Sec. III E 4, route 4 should provide reliable values of $\Delta\mu^{EC}_N$ since it is based on rigorous thermodynamic integration calculations. The only approximation made is the extrapolation of $\Delta\mu_N$ to $x^{eq}_{CO_2}$ on the solubility curve of CO_2 with the liquid at the corresponding temperature. However, we think this is a good approach taking into account the low values of the concentration and the results represented in Figs. 13 and 14. As can be seen in Fig. 15, small differences are seen between results obtained from routes 1 and 4. Route 1 slightly underestimates the driving force for nucleation in nearly the whole range of temperatures considered in this work, especially in the intermediate range of temperatures.

As in our previous work,[29] we have also used the dissociation route (route 3) according to Eq. (15), proposed by Kashchiev and Firoozabadi.[53] Agreement between the results from routes 3 and 4 is good, especially at low supercoolings. The dissociation route overestimates the values of $\Delta\mu^{EC}_N$ obtained from route 4 about $0.1k_BT$ at 260 K, approximately. This represents a value 6.5% higher than the value obtained from route 4, the maximum difference found between both approaches in the whole range of temperatures.

Finally, we have also obtained $\Delta\mu^{EC}_N$, as a function of the temperature, via route 2 proposed by us in our previous work[29] and inspired by the work of Molinero *et al.*[31] This route, given by Eq. (13), entails crude approximations. As can be seen, route 2 is not able to provide reliable predictions of $\Delta\mu^{EC}_N$ in the whole range of supercoolings. In fact, at 260 K its absolute value is about 20% smaller (i.e., around $0.32k_BT$) than that obtained from the most rigorous route 4. This result is in agreement with the findings observed in Figs. 13 and 14, and it is a direct consequence of the main approximation made in route 2: that the activity coefficients of water and CO_2 are equal to one. Although this is a good approximation for the methane hydrate,[29] it is not a realistic option for the CO_2 hydrate. The root of this behavior must be found in large differences in solubility of methane in water compared with that of CO_2 in water (in contact with both the gas/liquid phase and the hydrate phase). See Figs. 3 and 7 and the corresponding insets.

In summary, route 2 is not, in general, a good choice for calculating driving forces for nucleation of hydrates. This route can be used when the solubility of guest molecules in water is extremely low. Route 3 is an easy and fast way to estimate $\Delta\mu^{EC}_N$ values. However, we do not recommend this route, in general, except for temperatures close to T_3. Finally, route 4 is proposed here in the most rigorous and nearly exact way to evaluate driving forces for nucleation of hydrates.

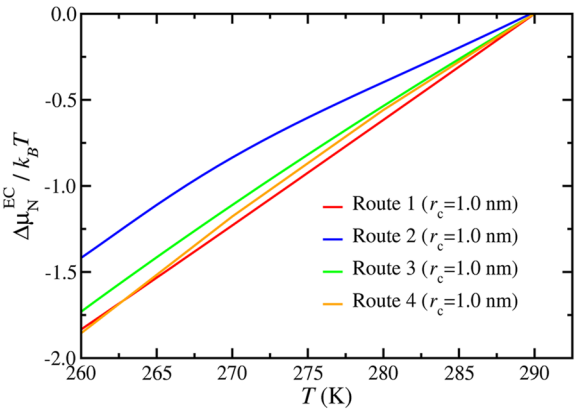

FIG. 15. Driving force for nucleation of the CO_2 hydrate at experimental conditions, as a function of the temperature along the 400 bar isobar with $r_c = 1.0$ nm and $T_3 = 290$ K, using route 1 (red curve), route 2 (blue curve), route 3 (green curve), and route 4 (orange curve).

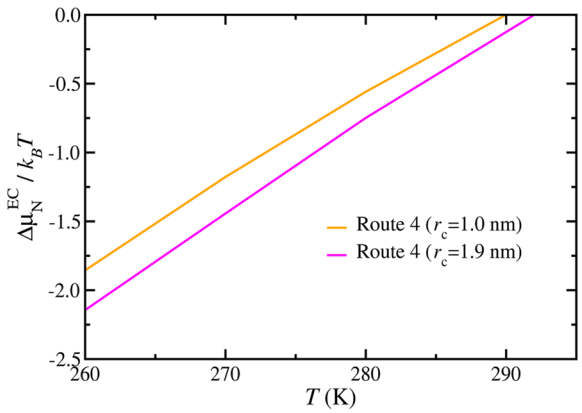

FIG. 16. Driving force for nucleation of the CO_2 hydrate at experimental conditions as a function of the temperature along the 400 bar isobar using route 4 with cutoff distances $r_c = 1.0$ (orange curve) and 1.9 nm (magenta curve).

Downloaded from http://pubs.aip.org/aip/jcp/article-pdf/doi/10.1063/5.0146618/17414902/184703_1_5.0146618.pdf

Published under an exclusive license by AIP Publishing

It is important to discuss the effect of the cutoff distance due to the dispersive interactions on $\Delta\mu_N^{EC}$. We have already analyzed the effect of r_c on the solubility curve of CO_2 in contact with both the CO_2 liquid (Fig. 3) and the hydrate (Fig. 7). Although the solubility curve of CO_2 with the hydrate is practically unaffected when r_c is changed from 1.0 to 1.9 nm, the situation is completely different for the solubility curve of CO_2 with the liquid. As a consequence of this, T_3 of the CO_2 hydrate changes from 290(2) K when r_c = 1.0 nm to 292(2) K when r_c = 1.9 nm. Obviously, this change must also affect the values of $\Delta\mu_N^{EC}$. We have obtained the driving force for nucleation following route 4 using a cutoff distance r_c = 1.9 nm, and results are compared with those using r_c = 1.0 nm. As can be seen in Fig. 16, the main effect is to displace the curve toward higher temperatures. This is an expected result due to the difference in the T_3 values using different cutoff distances. However, it is clearly seen that differences between both curves increase as the temperature is decreased: the difference between both values in absolute value is $0.125k_BT$ at 290 K, approximately, but that difference increases up to $0.286k_BT$ at 260 K, approximately. This is more than double of the value of the difference predicted at 290 K, suggesting that the increase of the cutoff distance has a deep effect on the driving force for nucleation of the system.

To check the real impact of the cutoff distance of the dispersive interaction on the driving force for nucleation, we have plot $\Delta\mu_N^{EC}$, as a function of the supercooling ΔT, instead of the absolute temperature T. This allows us to compare both results at the same supercooling and to have a clearer picture of this effect. As can be seen in Fig. 17, there is an important effect on $\Delta\mu_N^{EC}$ when r_c is changed from 1.0 to 1.9 nm. For instance, at $|\Delta T| \approx 25$ K, $\Delta\mu_N^{EC}$ changes from −1.5 to $-1.65k_BT$ when the cutoff distance is increased. According to this, the driving force for nucleation of the hydrate is 10% larger when r_c = 1.9 nm than that obtained using 1.0 nm. This effect is not negligible. The origin of this displacement is due to the strong dependence of the solubility of CO_2 in water on r_c (aqueous solution in contact with the CO_2 liquid phase). Due to the effect of the cutoff distance on $\Delta\mu_N^{EC}$, appropriate values of r_c are required in order to obtain reliable values of this magnitude.

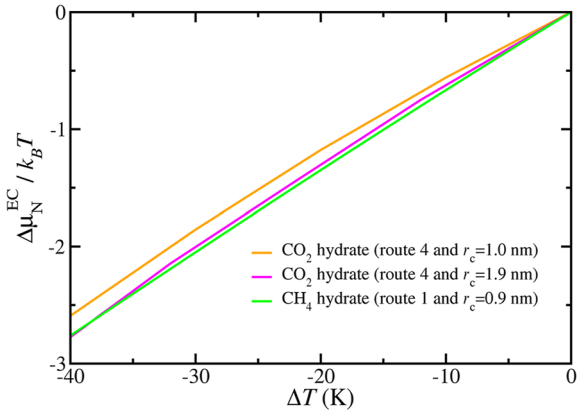

FIG. 17. Driving force for nucleation of the CO_2 hydrate at experimental conditions as a function of the supercooling ΔT along the 400 bar isobar with r_c = 1.0 nm (orange curve) and 1.9 nm (magenta curve) obtained using route 4 in both cases. The driving force for nucleation of the methane hydrate along the same isobar with r_c = 0.9 nm is also shown (green curve).[29] The dissociation temperatures in each case are T_3 = 290 (CO_2 hydrate with r_c = 1.0 nm), 292 (CO_2 hydrate with r_c = 1.9 nm), and 295 K (methane hydrate with r_c = 0.9 nm).

It is also very interesting to compare the driving force for the nucleation of the CO_2 and methane hydrates at the same pressure. We have determined in our previous work[29] the driving force at experimental conditions along the same isobar. We also present these results in Fig. 17, obtained using route 1 and a cutoff distance of r_c = 0.9 nm. We compare these results with those obtained for the CO_2 hydrate using a cutoff distance of 1.0 nm. As can be seen, the driving force of the CO_2 hydrate is in absolute value, lower than that of the methane hydrate along the isobar of 400 bar. For instance, at a supercooling of $|\Delta T| \approx 25$ K, the driving force for the methane hydrate is $\Delta\mu_N^{EC} \approx -1.7\,k_BT$. At the same supercooling for CO_2, $\Delta\mu_N^{EC} \approx -1.5\,k_BT$. This means that the driving force for the nucleation of the CO_2 hydrate, at 400 bar, is 13% lower than that of the methane hydrate at the same supercooling (ΔT = 25 K). According to this, the nucleation of the methane hydrate should be more favorable than that of the CO_2 hydrate. Obviously, this would be true if the other factors that affect the nucleation rate of the hydrates are equal, i.e., the water–hydrate interfacial energy (which may not be the case).

We have also considered the effect of the occupancy of CO_2 in the hydrate on the driving force for nucleation. Particularly, we study hydrates with 7 CO_2 molecules per unit cell, i.e., 50% of occupancy in the small or D cages and 100% of occupancy in the large or T cages, which is equivalent to 87.5% of overall occupancy. According to the work of Kashchiev and Firoozabadi,[53] the formation of a hydrate in the aqueous solution phase can be described as the chemical reaction of Eq. (7). This reaction can be viewed as the formation of a "hydrate molecule" per each CO_2 molecule in the aqueous solution.

However, since we now calculate and compare driving forces for nucleation of hydrates with different occupancies, it is more convenient to write Eq. (7) per cage of hydrate formed from the aqueous solution than per CO_2 molecule used to form the hydrate from the solution. In the case of a hydrate fully occupied, the reaction is the same in both descriptions since a unit cell of hydrate is formed from eight cages (6 T and 2 D cages) and it is occupied by eight CO_2 molecules as well. Let us define the occupancy x_{occ} as the fraction of cages occupied by CO_2, $x_{occ} = n_{CO_2}/n_{cg}$, where n_{CO_2} and n_{cg} are the number of CO_2 molecules and cages per unit cell. When the occupancy is 100%, $x_{occ} = 8/8 = 1$ and $x_{occ} = 7/8 = 0.875$ when it is 87.5%. According to this, the formation of one cage of hydrate, with occupancy 87.5%, from the aqueous solution phase can be viewed as a classical chemical reaction that takes place at constant P and T,

$$x_{occ}\,CO_2(aq) + 5.75\,H_2O(aq) \longrightarrow [(CO_2)_{x_{occ}}(H_2O)_{5.75}]_H. \quad (27)$$

In this particular case, since each unit cell of CO_2 hydrate is formed from n_{cg} = 8 cages and 46 water molecules, we only need 7/8 = 0.875 CO_2 molecules (i.e., an occupancy $x_{occ} = 7/8 = 0.875$) and 46/8 = 5.75 water molecules in the solution to form one cage of hydrate with the desired occupancy (seven CO_2 molecules per unit cell). The compound $[(CO_2)_{x_{occ}}(H_2O)_{5.75}]_H$ is simply a "cage" of hydrate. According to this, we call $[(CO_2)_{x_{occ}}(H_2O)_{5.75}]$ a

Downloaded from http://pubs.aip.org/aip/jcp/article-pdf/doi/10.1063/5.0146618/17414902/184703_1_5.0146618.pdf

Published under an exclusive license by AIP Publishing

"molecule" of one cage of the hydrate in the solid. Note that stoichiometry of reaction given by Eq. (27) is in agreement with a unit cell of this partially occupied hydrate, formed from eight "cages" of hydrate with $8 \times 0.875 = 7$ CO_2 molecules and $8 \times 5.75 = 46$ water molecules.

We have used route 1 described in Sec. III E 1 with a cutoff distance for the dispersive interactions of $r_c = 1.0$ nm. We have followed the same procedure previously explained, but instead of simulating a hydrate fully occupied by CO_2 molecules, we have considered a hydrate with occupancy of the small or D cages of 50% (87.5% overall occupancy of the hydrate). To be consistent with the description of the previous paragraph, we have used Eq. (11) to evaluate the driving force for nucleation of the partially occupied hydrate per cage of hydrate instead of per CO_2 molecule. According to this, the corresponding molar enthalpy of the hydrate, h_H^H, as a function of the temperature, must be expressed as an enthalpy per cage of the hydrate, $\tilde{h}_H^H$,

$$h_H^H = \frac{H}{N_{CO_2}} = \frac{H}{N_{cg}}\left(\frac{N_{cg}}{N_{CO_2}}\right) = \tilde{h}_H^H\left(\frac{N_{cg}}{N_{CO_2}}\right) = \frac{\tilde{h}_H^H}{x_{occ}}. \quad (28)$$

Here, H is the enthalpy of the hydrate and N_{CO_2} and N_{cg} are the total number of CO_2 molecules and cages used in simulations, respectively. $N_{CO_2} = n_{cells} \times n_{CO_2}$ and $N_{cg} = n_{cells} \times n_{cg}$, with $n_{cells} = 3 \times 3 \times 3 = 27$ being the number of unit cells in simulations. Note that the enthalpy per cage, $\tilde{h}_H^H$, is obtained dividing the enthalpy of the hydrate by the total number of cages, $N_{cg} = n_{cells} \times n_{cg} = 27 \times 8 = 216$. H is calculated in the same way as in Sec. III E 1 for the fully occupied hydrate but now using a simulation box with 189 CO_2 molecules and 27 replicas of the unit cell in a $3 \times 3 \times 3$ geometry used in Sec. III E 1 for the 1242 water molecules.

Figure 18 shows the enthalpy per cage of the hydrate $\tilde{h}_H^H$ partially occupied by CO_2 molecules as a function of temperature (blue diamonds). We also present the enthalpy per cage of the hydrate with 100% of occupancy (red circles). Note that $\tilde{h}_H^H$ is equal to the enthalpy of the hydrate per molecule of CO_2, h_H^H, in the case of full occupancy.

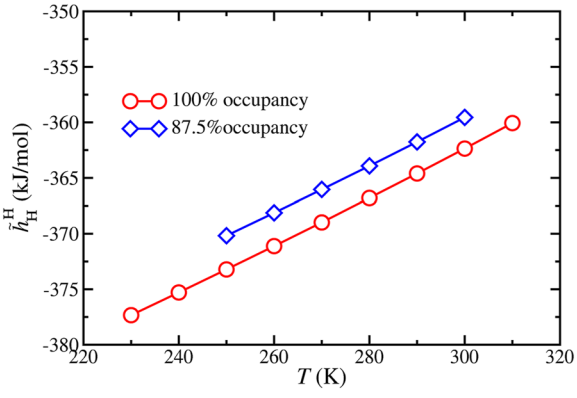

FIG. 18. Enthalpy per cage of the CO_2 hydrate at 400 bar, $\tilde{h}_H^H$, as a function of temperature with 100% of occupancy (red circles) and with 87.5% of occupancy (blue diamonds). The lines are guides to the eye. Note that for the case of 100% occupancy, the enthalpy per cage of the hydrate is identical to the enthalpy per CO_2 molecule, but this is not the case when the occupancy is lower. The continuous curves are guides to the eyes.

As can be seen, the enthalpy per cage when occupancy is 87.5% is systematically less negative than $\tilde{h}_H^H$ when the hydrate is fully occupied. The difference between both values is ~3 kJ/mol. This is an expected result since there is one CO_2 molecule less per unit cell (7 instead of 8) in the hydrate with an occupancy of 87.5%. Although the difference is below 1%, there is less CO_2–water favorable (negative) dispersive interactions, and this contributes to increase the energy and consequently the enthalpy of the system. Note that the lattice parameters of the unit cell (for a certain P and T) of the hydrate depend on the occupancy. Particularly, it becomes about 0.16% smaller when the occupancy changes from 100% to 87.5%.

Once $\tilde{h}_H^H(T)$ is known, it is possible to use Eq. (11) to evaluate the driving force for nucleation of the hydrate. However, Eq. (11) is only valid for hydrates with 100% occupancy. It is possible to reformulate route 1 for hydrates partially occupied taking into account that the enthalpy of the hydrate is expressed per cage of the hydrate, $\tilde{h}_H^H$, and using the appropriate stoichiometry when the hydrate has an occupancy of x_{occ}. According to this, the driving force for nucleation per cage of hydrate is given by

$$\frac{\Delta\mu_N^{EC}(T, x_{CO_2}^{eq})}{k_B T} = -\int_{T_3}^{T} \frac{\tilde{h}_H^H(T') - \{x_{occ}\, h_{CO_2}^{pure}(T') + 5.75 h_{H_2O}^{pure}(T')\}}{k_B T'^2} dT' - \left[k_B T \ln\{x_{H_2O}^{eq}(T)\} - k_B T_3 \ln\{x_{H_2O}^{eq}(T_3)\}\right]. \quad (29)$$

Note that Eq. (29) is consistent with the view of Kashchiev and Firoozabadi[53] and with the reaction given by Eq. (27) in which the hydrate is a new compound formed from x_{occ} molecules of CO_2 and 5.75 molecules of water when the hydrate occupancy is x_{occ}. We should also remind that the value of T_3 was not affected (within our error bar) by the occupancy of the hydrate as it was shown in Fig. 8 so that the value of $T_3 = 290$ K will be used regardless of the occupancy.

Figure 19 shows the comparison between the driving force for nucleation obtained using route 1 and a cutoff distance of

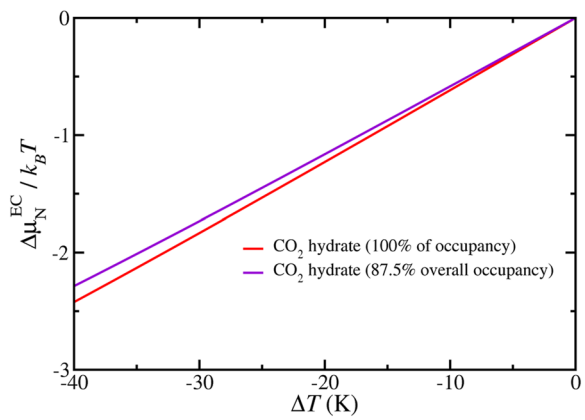

FIG. 19. Driving force for nucleation of the CO_2 hydrate at experimental conditions, as a function of the supercooling ΔT along the 400 bar isobar, with $r_c = 1.0$ nm when the hydrate is fully occupied by CO_2 molecules (red curve) and when the occupancy of the small or D cages is 50% (87.5% overall occupancy) (magenta curve) obtained using route 1 in both cases.

Downloaded from http://pubs.aip.org/aip/jcp/article-pdf/doi/10.1063/5.0146618/17414902/184703_1_5.0146618.pdf

Published under an exclusive license by AIP Publishing

r_c = 1.0 nm when the hydrate is fully occupied and when only half of the small or D cages are occupied by CO_2 molecules. It is important to remark here that we are calculating driving forces for nucleation per cage of hydrate. This allows us to compare $\Delta\mu_N^{EC}$ for both hydrates at the same conditions since the number of water molecules that form both solids is the same. Particularly, it is possible to know if a hydrate fully occupied is thermodynamically more stable than a hydrate partially occupied (87.5%) when both are formed from an aqueous solution of CO_2 at fixed conditions of pressure and temperature.

As can be seen, $\Delta\mu_N^{EC}$ is similar in both cases for low supercoolings. However, as the supercooling increases, the differences between both values increase. Particularly, $\Delta\mu_N^{EC}$ becomes less negative (driving force for nucleation is lower) when the hydrate is partially occupied than when the hydrate is fully occupied. This means that the fully occupied hydrate is more stable, from the thermodynamic point of view, than the hydrate with an occupancy of 87.5% since the driving force for nucleation is higher. However, it remains to be studied in the future if an occupancy between 0.875 and 1 could be more stable than the fully occupied hydrate.

IV. CONCLUSIONS

In this work, we have studied the solubility of CO_2 in aqueous solutions when they are in contact via planar interfaces with a CO_2-rich liquid phase and with the hydrate phase at 400 bar using molecular dynamics computer simulations. We have also estimated the driving force for the nucleation of the CO_2 hydrate using four different routes. These properties are key to understanding, from a thermodynamics point of view, the parameters that control the nucleation of CO_2 hydrates. Water is described using the TIP4P/Ice water model and CO_2 using the TraPPE model. The unlike dispersive interactions between water and CO_2 are taken into account using the approach proposed by us several years ago. This selection allows us to describe very accurately not only the dissociation temperature of the hydrate at the pressure considered in this work but also the CO_2 hydrate–water interfacial free energy. Calculations of solubilities have been carried out using the direct coexistence technique between two phases. Additional simulations of the pure systems, at several temperatures, have also been performed to calculate the driving force for nucleation along the isobar considered in this work.

We have analyzed the aqueous solution of CO_2 when it is in contact with the liquid phase (pure CO_2) and with the hydrate using two different values of the cutoff associated with the dispersive interactions. From this information, we have obtained the solubility of CO_2 in water when the solution is in contact with the CO_2 liquid phase. The solubility of CO_2 decreases with temperature, in a similar way to that of methane. However, the solubility of CO_2 is one order of magnitude larger than that of methane. We also observed an important effect of long-range dispersive interactions in the solubility curve along the isobar of 400 bar. The solubility of methane in water is also affected by these contributions, but their effect is smaller. It is interesting to remark that corrections due to long-range dispersive interactions affect in a different way both systems. Whereas the solubility of CO_2 increases with the cutoff distance, in the case of methane, it decreases. This is probably an effect due to the CO_2–CO_2 and CO_2–water electrostatic interactions. We have also studied the solubility of CO_2 in the aqueous solution when it is in contact with the hydrate and analyzed its interfacial structure. This magnitude increases with the temperature, as it happens with the solubility of methane in water. Contrary to what happens when the aqueous solution is in contact with the CO_2 liquid phase, the variation of the cutoff distance due to the long-range dispersive interaction has no effect on the solubility. This behavior has also been observed in our previous study dealing with the solubility of methane in water.

The dissociation temperature of the CO_2 hydrate (T_3), at 400 bar, can be evaluated from the intersection of the two solubility curves obtained in this work. This intersection is possible because the formation of the hydrate phase, at $T < T_3$, and the formation of the CO_2 liquid phase, at $T > T_3$, are activated processes. This means that there exists metastability below and above the dissociation temperature of the hydrate at 400 bar, and because of this, one can find the intersection between the two solubility curves. The temperature at which this occurs is T_3 of the hydrate at the fixed pressure. From this analysis, we find that the dissociation temperature of the hydrate is located at 290(2) K when the cutoff distance for dispersive interactions is equal to 1.0 nm. This is in good agreement (within the error bars) with our previous estimation of T_3 obtained from direct coexistence simulations and using the same cutoff distance, 287(2) K. If the cutoff distance is larger (1.9 nm), T_3 is located at 292(2) K. Although the value obtained in this work for a cutoff distance of 1.0 nm compares well with our previous estimation, 287(2) K (within the error bars), it is possible that finite-size effects produce a shift of T_3 toward higher temperatures, as well as the value used to account for long-range dispersive interactions.

We also estimate the driving force for nucleation of the CO_2 hydrate. Particularly, we have calculated $\Delta\mu_N$ using the three routes proposed in our previous paper (routes 1–3).[29] Since the solubility of CO_2 in water is higher than that of methane by one order of magnitude, we have proposed a novel and alternative route based on the use of the solubility curve of CO_2 with the hydrate. This new route (which we refer to as route 4 in this paper) considers rigorously the non-ideality of the aqueous solution of CO_2 and provides reliable results for $\Delta\mu_N$. Routes 1, 3, and 4 provide similar values of the driving force for nucleation of the CO_2 hydrate in a wide range of supercoolings. Unfortunately, route 2 cannot be used for CO_2 hydrates due to the non-ideality of the water + CO_2 mixture at the conditions considered.

Finally, we have also analyzed the effect of the cutoff distance due to dispersive interactions and the occupancy of the cages on the driving force for nucleation of the CO_2 hydrate. In both cases, there is a non-negligible effect on the driving force for nucleation. Particularly, the driving force for nucleation increases when the cutoff distance increases and when the occupancy of the small or D cages of the hydrate increases from 87.5% of occupancy to 100%.

ACKNOWLEDGMENTS

This work was financed by the Ministerio de Ciencia e Innovación (Grant No. PID2021-125081NB-I00), the Junta de Andalucía (P20-00363), and the Universidad de Huelva (Grant Nos. P.O. FEDER UHU-1255522 and FEDER-UHU-202034),

Downloaded from http://pubs.aip.org/aip/jcp/article-pdf/doi/10.1063/5.0146618/17414902/184703_1_5.0146618.pdf

Published under an exclusive license by AIP Publishing

all four cofinanced by EU FEDER funds. We also acknowledge the Centro de Supercomputación de Galicia (CESGA, Santiago de Compostela, Spain) for providing access to computing facilities. We also acknowledge Project No. PID2019-105898GB-C21 from the Ministerio de Educación y Cultura. We also acknowledge access to supercomputer time from RES through Project No. FI-2022-1-0019. J.G. acknowledges the national support from the Gdansk University of Technology by Grant No. DEC-09/2021/IDUB/II.1/AMERICIUM/ZD under the AMERICIUM—"Excellence Initiative-Research University" program. Part of the computations were carried out at the Centre of Informatics Tricity Academic Supercomputer and Network. This research was supported, in part, by PL-Grid Infrastructure.

AUTHOR DECLARATIONS

Conflict of Interest

The authors have no conflicts to disclose.

Author Contributions

Jesús Algaba: Conceptualization (equal); Data curation (lead); Formal analysis (lead); Investigation (equal); Writing – original draft (equal); Writing – review & editing (equal). **Iván M. Zerón**: Conceptualization (lead); Data curation (equal); Investigation (equal); Methodology (equal); Supervision (equal); Writing – review & editing (equal). **José Manuel Míguez**: Conceptualization (equal); Data curation (equal); Investigation (equal); Methodology (equal); Writing – review & editing (equal). **Joanna Grabowska**: Investigation (equal); Methodology (equal); Writing – review & editing (equal). **Samuel Blazquez**: Investigation (equal); Methodology (equal); Writing – review & editing (equal). **Eduardo Sanz**: Investigation (equal); Methodology (equal); Writing – review & editing (equal). **Carlos Vega**: Conceptualization (equal); Investigation (equal); Methodology (equal); Writing – review & editing (equal). **Felipe J. Blas**: Conceptualization (lead); Investigation (lead); Methodology (equal); Supervision (equal); Writing – original draft (equal); Writing – review & editing (equal).

DATA AVAILABILITY

The data that support the findings of this study are available within the article.

REFERENCES

[1]D. Eisenberg and W. Kauzmann, *The Structure and Properties of Water* (Oxford University Press, 1969).
[2]V. F. Petrenko and R. W. Whitworth, *Physics of Ice* (Oxford University Press, 1999).
[3]E. Sanz, C. Vega, J. L. F. Abascal, and L. G. MacDowell, "Phase diagram of water from computer simulation," Phys. Rev. Lett. **92**, 255701 (2004).
[4]E. D. Sloan and C. Koh, *Clathrate Hydrates of Natural Gases*, 3rd ed. (CRC Press, New York, 2008).
[5]K. A. Kvenvolden, "Methane hydrate—A major reservoir of carbon in the shallow geosphere?," Chem. Geol. **71**, 41–51 (1988).
[6]C. A. Koh, A. K. Sum, and E. D. Sloan, "State of the art: Natural gas hydrates as a natural resource," J. Nat. Gas Sci. Eng. **8**, 132–138 (2012).
[7]M. Yang, Y. Song, L. Jiang, Y. Zhao, X. Ruan, Y. Zhang, and S. Wang, "Hydrate-based technology for CO_2 capture from fossil fuel power plants," Appl. Energy **116**, 26–40 (2014).
[8]M. Ricaurte, C. Dicharry, X. Renaud, and J.-P. Torré, "Combination of surfactants and organic compounds for boosting CO_2 separation from natural gas by clathrate hydrate formation," Fuel **122**, 206–217 (2014).
[9]B. Kvamme, A. Graue, T. Buanes, T. Kuznetsova, and G. Ersland, "Storage of CO_2 in natural gas hydrate reservoirs and the effect of hydrate as an extra sealing in cold aquifers," Int. J. Greenhouse Gas Control **1**, 236–246 (2007).
[10]D. M. D'Alessandro, B. Smit, and J. R. Long, "Carbon dioxide capture: Prospects for new materials," Angew. Chem., Int. Ed. **49**, 6058–6082 (2010).
[11]S. Choi, J. H. Drese, and C. W. Jones, "Adsorbent materials for carbon dioxide capture from large anthropogenic point sources," ChemSusChem **2**, 796–854 (2009).
[12]J. C. Platteeuw and J. H. van der Waals, "Thermodynamic properties of gas hydrates," Mol. Phys. **1**, 91–96 (1957).
[13]J. C. Platteeuw and J. H. van der Waals, "Thermodynamic properties of gas hydrates II: Phase equilibria in the system H_2S-C_3H_3-H_2O at −3 °C," Rec. Trav. Chim. Pays Bas **78**, 126–133 (1959).
[14]C. A. Koh, "Towards a fundamental understanding of natural gas hydrates," Chem. Soc. Rev. **31**, 157–167 (2002).
[15]I. N. Tsimpanogiannis and I. G. Economou, "Monte Carlo simulation studies of clathrate hydrates: A review," J. Supercrit. Fluids **134**, 51–60 (2018).
[16]V. K. Michalis, J. Costandy, I. N. Tsimpanogiannis, A. K. Stubos, and I. G. Economou, "Prediction of the phase equilibria of methane hydrates using the direct phase coexistence methodology," J. Chem. Phys. **142**, 044501 (2015).
[17]J. Costandy, V. K. Michalis, I. N. Tsimpanogiannis, A. K. Stubos, and I. G. Economou, "The role of intermolecular interactions in the prediction of the phase equilibria of carbon dioxide hydrates," J. Chem. Phys. **143**, 094506 (2015).
[18]V. K. Michalis, I. N. Tsimpanogiannis, A. K. Stubos, and I. G. Economou, "Direct phase coexistence molecular dynamics study of the phase equilibria of the ternary methane-carbon dioxide-water hydrate system," Phys. Chem. Chem. Phys. **18**, 23538–23548 (2016).
[19]M. H. Waage, T. J. H. Vlugt, and S. Kjelstrup, "Phase diagram of methane and carbon dioxide hydrates computed by Monte Carlo simulations," J. Phys. Chem. B **121**, 7336–7350 (2017).
[20]M. M. Conde and C. Vega, "Determining the three-phase coexistence line in methane hydrates using computer simulations," J. Chem. Phys. **133**, 064507 (2010).
[21]M. M. Conde and C. Vega, "Note: A simple correlation to locate the three phase coexistence line in methane-hydrate simulations," J. Chem. Phys. **138**, 056101 (2013).
[22]J. M. Míguez, M. M. Conde, J.-P. Torré, F. J. Blas, M. M. Piñeiro, and C. Vega, "Molecular dynamics simulation of CO_2 hydrates: Prediction of three phase coexistence line," J. Chem. Phys. **142**, 124505 (2015).
[23]M. Pérez-Rodríguez, A. Vidal-Vidal, J. M. Míguez, F. J. Blas, J.-P. Torré, and M. M. Piñeiro, "Computational study of the interplay between intermolecular interactions and CO_2 orientations in type I hydrates," Phys. Chem. Chem. Phys. **19**, 3384–3393 (2017).
[24]A. M. Fernández-Fernández, M. Pérez-Rodríguez, A. Comesaña, and M. M. Piñeiro, "Three-phase equilibrium curve shift for methane hydrate in oceanic conditions calculated from molecular dynamics simulations," J. Mol. Liq. **274**, 426–433 (2019).
[25]P. Thoutam, S. Rezaei Gomari, F. Ahmad, and M. Islam, "Comparative analysis of hydrate nucleation for methane and carbon dioxide," Molecules **24**, 1055 (2021).
[26]J. R. Espinosa, C. Vega, C. Valeriani, and E. Sanz, "Seeding approach to crystal nucleation," J. Chem. Phys. **144**, 034501 (2016).
[27]P. G. Debenedetti, *Metastable Liquids: Concepts and Principles* (Princeton University Press, 1997).
[28]G. D. Soria, J. R. Espinosa, J. Ramirez, C. Valeriani, C. Vega, and E. Sanz, "A simulation study of homogeneous ice nucleation in supercooled salty water," J. Chem. Phys. **148**, 222811 (2018).
[29]J. Grabowska, S. Blázquez, E. Sanz, I. M. Zerón, J. Algaba, J. M. Míguez, F. J. Blas, and C. Vega, "Solubility of methane in water: Some useful results for hydrate nucleation," J. Phys. Chem. B **126**, 8553–8570 (2022).

Downloaded from http://pubs.aip.org/aip/jcp/article-pdf/doi/10.1063/5.0146618/17414902/184703_1_5.0146618.pdf

Published under an exclusive license by AIP Publishing

[30]J. Grabowska, S. Blázquez, E. Sanz, E. G. Noya, I. M. Zerón, J. Algaba, J. M. Míguez, F. J. Blas, and C. Vega, "Homogeneous nucleation rate of methane hydrate formation under experimental conditions from seeding simulations," J. Chem. Phys. **158**, 114505 (2023).
[31]B. C. Knott, V. Molinero, M. F. Doherty, and B. Peters, "Homogeneous nucleation of methane hydrates: Unrealistic under realistic conditions," J. Am. Chem. Soc. **134**, 19544–19547 (2012).
[32]V. Molinero and E. B. Moore, "Water modeled as an intermediate element between carbon and silicon," J. Phys. Chem. B **113**, 4008–4016 (2009).
[33]L. C. Jacobson, W. Hujo, and V. Molinero, "Amorphous precursors in the nucleation of clathrate hydrates," J. Am. Chem. Soc. **132**, 11806–11811 (2010).
[34]L. C. Jacobson, W. Hujo, and V. Molinero, "Nucleation pathways of clathrate hydrates: Effect of guest size and solubility," J. Phys. Chem. B **114**, 13796–13807 (2010).
[35]L. C. Jacobson and V. Molinero, "Can amorphous nuclei grow crystalline clathrates? The size and crystallinity of critical clathrate nuclei," J. Am. Chem. Soc. **133**, 6458–6463 (2011).
[36]S. Sarupria and P. G. Debenedetti, "Molecular dynamics study of carbon dioxide hydrate dissociation," J. Phys. Chem. Lett. **3**, 2942–2947 (2012).
[37]S. Sarupria and P. G. Debenedetti, "Homogeneous nucleation of methane hydrate in microsecond molecular dynamics simulations," J. Phys. Chem. A **115**, 6102–6111 (2011).
[38]D. Yuhara, B. C. Barnes, D. Suh, B. C. knott, G. T. Beckham, K. Yasuoka, D. T. Wu, and A. K. Sum, "Nucleation rate analysis of methane hydrate from molecular dynamics simulations," Faraday Discuss. **179**, 463–474 (2015).
[39]S. Liang and P. G. Kusalik, "Nucleation of gas hydrates within constant energy systems," J. Phys. Chem. B **117**, 1403 (2013).
[40]B. C. Barnes, B. C. Knott, G. T. Beckham, D. T. Wu, and A. K. Sum, "Molecular dynamics study of carbon dioxide hydrate dissociation," J. Phys. Chem. B **118**, 13236–13243 (2014).
[41]M. R. Walsh, G. T. Beckham, C. A. Koh, E. D. Sloan, D. T. Wu, and A. K. Sum, "Methane hydrate nucleation rates from molecular dynamics simulations: Effects of aqueous methane concentration, interfacial curvature, and system size," J. Phys. Chem. C **115**, 21241 (2011).
[42]P. Warrier, M. N. Khan, V. Srivastava, C. M. Maupin, and C. A. Koh, "Overview: Nucleation of clathrate hydrates," J. Chem. Phys. **145**, 211705 (2016).
[43]Z. Zhang, C.-J. Liu, M. R. Walsh, and G.-J. Guo, "Effects of ensembles on methane hydrate nucleation kinetics," Phys. Chem. Chem. Phys. **18**, 15602 (2016).
[44]M. Lauricella, G. Ciccotti, N. J. English, B. Peters, and S. Meloni, "Mechanisms and nucleation rate of methane hydrate by dynamical nonequilibrium molecular dynamics," J. Phys. Chem. C **121**, 24223 (2016).
[45]Arjun, T. A. Berendsen, and P. G. Bolhuis, "Unbiased atomistic insight in the competing nucleation mechanisms of methane hydrates," Proc. Natl. Acad. Sci. U. S. A. **116**, 19305 (2019).
[46]T. Karmakar, P. M. Piaggi, and M. Parrinello, "Molecular dynamics simulations of crystal nucleation from solution at constant chemical potential," J. Chem. Theory Comput. **15**, 6923 (2019).
[47]A. Arjun and P. G. Bolhuis, "Rate prediction for homogeneous nucleation of methane hydrate at moderate supersaturation using transition interface sampling," J. Phys. Chem. B **124**, 8099 (2020).
[48]A. Arjun and P. G. Bolhuis, "Homogenous nucleation rate of CO_2 hydrates using transition interface sampling," J. Chem. Phys. **154**, 164507 (2021).
[49]G.-J. Guo and Z. Zhang, "Open questions on methane hydrate nucleation," Commun. Chem. **4**, 102 (2021).
[50]B. Kvamme, S. A. Aromada, N. Saeidi, T. Hustache-Marmou, and P. Gjerstad, "Hydrate nucleation, growth, and induction," ACS Omega **5**, 2603 (2020).
[51]M. C. dos Ramos, F. J. Blas, and A. Galindo, "Phase equilibria, excess properties, and Henry's constants of the water + carbon dioxide binary mixture," J. Chem. Phys. **111**, 015924–15934 (2007).
[52]D. Kashchiev, *Nucleation* (Butterworth-Heinemann, Oxford, UK, 2000).
[53]D. Kashchiev and A. Firoozabadi, "Driving force for crystallization of gas hydrates," J. Cryst. Growth **241**, 220–230 (2002).
[54]D. Kashchiev and A. Firoozabadi, "Nucleation of gas hydrates," J. Cryst. Growth **243**, 476–489 (2002).
[55]D. Kashchiev and G. M. van Rosmalen, "Review: Nucleation in solutions revisited," Cryst. Res. Technol. **38**, 555–574 (2003).
[56]D. van der Spoel, E. Lindahl, B. Hess, G. Groenhof, A. E. Mark, and H. J. C. Berendsen, "GROMACS: Fast, flexible, and free," J. Comput. Chem. **26**, 1701–1718 (2005).
[57]L. J. Chen, "Area dependence of the surface tension of a Lennard-Jones fluid from molecular dynamics simulations," J. Chem. Phys. **103**, 10214 (1995).
[58]M. González-Melchor, P. Orea, J. López-Lemus, F. Bresme, and J. Alejandre, "Stress anisotropy induced by periodic boundary conditions," J. Chem. Phys. **122**, 094503 (2005).
[59]J. Janeček, "Effect of the interfacial area on the equilibrium properties of Lennard-Jones fluid," J. Chem. Phys. **131**, 124513 (2009).
[60]M. A. Cuendet and W. F. van Gunsteren, "On the calculation of velocity-dependent properties in molecular dynamics simulations using the leapfrog integration algorithm," J. Chem. Phys. **127**, 184102 (2007).
[61]S. Nosé, "A molecular dynamics method for simulations in the canonical ensemble," Mol. Phys. **52**, 255–268 (1984).
[62]M. Parrinello and A. Rahman, "Polymorphic transitions in single crystals: A new molecular dynamics method," J. Appl. Phys. **52**, 7182–7190 (1981).
[63]U. Essmann, L. Perera, M. L. Berkowitz, T. Darden, H. Lee, and L. G. Pedersen, "A smooth particle mesh Ewald method," J. Chem. Phys. **103**, 8577–8593 (1995).
[64]J. L. Abascal, E. Sanz, R. G. Fernández, and C. Vega, "A potential model for the study of ices and amorphous water: TIP4P/Ice," J. Chem. Phys. **122**, 234511 (2005).
[65]J. J. Potoff and J. I. Siepmann, "Vapor-liquid equilibria of mixtures containing alkanes, carbon dioxide, and nitrogen," AIChE J. **47**, 1676–1682 (2001).
[66]J. Algaba, E. Acuña, J. M. Míguez, B. Mendiboure, I. M. Zerón, and F. J. Blas, "Simulation of the carbon dioxide hydrate-water interfacial energy," J. Colloid Interface Sci. **623**, 354–367 (2022).
[67]I. M. Zerón, J. M. Míguez, B. Mendiboure, J. Algaba, and F. J. Blas, "Simulation of the CO_2 hydrate–water interfacial energy: The mold integration–guest methodology," J. Chem. Phys. **157**, 134709 (2022).
[68]J. M. Míguez, J. M. Garrido, F. J. Blas, H. Segura, A. Mejía, and M. M. Piñeiro, "Comprehensive characterization of interfacial behavior for the mixture CO_2 + H_2O + CH_4: Comparison between atomistic and coarse grained molecular simulation models and density gradient theory," J. Phys. Chem. C **118**, 24504–24519 (2014).
[69]A. Trokhymchuk and J. Alejandre, "Computer simulations of liquid/vapor interface in Lennard-Jones fluids: Some questions and answers," J. Chem. Phys. **111**, 8510–8523 (1999).
[70]J. M. Míguez, M. M. Piñeiro, and F. J. Blas, "Influence of the long-range corrections on the interfacial properties of molecular models using Monte Carlo simulation," J. Chem. Phys. **138**, 034707 (2013).
[71]F. J. Martínez-Ruiz, F. J. Blas, B. Mendiboure, and A. I. Moreno-Ventas Bravo, "Effect of dispersive long-range corrections to the pressure tensor: The vapour-liquid interfacial properties of the Lennard-Jones system revisited," J. Chem. Phys. **141**, 184701 (2014).
[72]H. Hulshof, "Ueber die oberflachenspannung," Ann. Phys. **309**, 165–186 (1901).
[73]J. S. Rowlinson and B. Widom, *Molecular Theory of Capillarity* (Clarendon Press, 1982).
[74]E. De Miguel, F. J. Blas, and E. M. Del Río, "Molecular simulation of model liquid crystals in a strong aligning field," Mol. Phys. **104**, 2919–2927 (2006).
[75]E. de Miguel and G. Jackson, "The nature of the calculation of the pressure in molecular simulations of continuous models from volume perturbations," J. Chem. Phys. **125**, 164109 (2006).
[76]P. Chiquet, J.-L. Daridon, D. Broseta, and S. Thibeau, "CO_2/water interfacial tensions under pressure and temperature conditions of CO_2 geological storage," Energy Convers. Manag. **48**, 736–744 (2007).

Downloaded from http://pubs.aip.org/aip/jcp/article-pdf/doi/10.1063/5.0146618/17414902/184703_1_5.0146618.pdf

Published under an exclusive license by AIP Publishing

[77]J. Janeček, "Long range corrections in inhomogeneous simulations," J. Phys. Chem. B **110**, 6264–6269 (2006).
[78]V. K. Shen, R. D. Mountain, and J. R. Errington, "Comparative study of the effect of tail corrections on surface tension determined by molecular simulation," J. Phys. Chem. B **111**, 6198–6207 (2007).
[79]F. J. Blas, L. G. MacDowell, E. de Miguel, and G. Jackson, "Vapor-liquid interfacial properties of fully flexible Lennard-Jones chains," J. Chem. Phys. **129**, 144703 (2008).
[80]L. G. MacDowell and F. J. Blas, "Surface tension of fully flexible Lennard-Jones chains: Role of long-range corrections," J. Chem. Phys. **131**, 074705 (2009).
[81]R. W. Henning, A. J. Schultz, V. Thieu, and Y. Halpern, "Neutron diffraction studies of CO_2 clathrate hydrate: Formation from deuterated ice," J. Phys. Chem. A **104**, 5066 (2000).
[82]K. A. Udachin, C. I. Ratcliffe, and J. A. Ripmeester, "Structure, composition, and thermal expansion of CO_2 hydrate from single crystal X-ray diffraction measurements," J. Phys. Chem. B **105**, 4200 (2001).
[83]T. Ikeda, O. Yamamuro, T. Matsuo, K. Mori, S. Torii, T. Kamiyama, F. Izumi, S. Ikeda, and S. Mae, "Neutron diffraction study of carbon dioxide clathrate hydrate," J. Phys. Chem. Solids **60**, 1527 (1999).
[84]J. A. Ripmeester and C. I. Ratcliffe, "The diverse nature of dodecahedral cages in clathrate hydrates as revealed by ^{129}Xe and ^{13}C NMR spectroscopy: CO_2 as a small-cage guest," Energy Fuels **12**, 197 (1998).
[85]M. M. Conde, M. Rovere, and P. Gallo, "High precision determination of the melting points of water TIP4P/2005 and water TIP4P/Ice models by the direct coexistence technique," J. Chem. Phys. **147**, 244506 (2017).
[86]I. N. Levine, *Physical Chemistry* (McGraw-Hill, New York, 2009).

Downloaded from http://pubs.aip.org/aip/jcp/article-pdf/doi/10.1063/5.0146618/17414902/184703_1_5.0146618.pdf

Published under an exclusive license by AIP Publishing